



HAL
open science

Atomistic simulations of basal dislocations in Mg interacting with Mg₁₇Al₁₂ precipitates

Aviral Vaid, Julien Guénoilé, Aruna Prakash, Sandra Korte-Kerzel, Erik Bitzek

► **To cite this version:**

Aviral Vaid, Julien Guénoilé, Aruna Prakash, Sandra Korte-Kerzel, Erik Bitzek. Atomistic simulations of basal dislocations in Mg interacting with Mg₁₇Al₁₂ precipitates. *Materialia*, 2019, 7, pp.100355. 10.1016/j.mtla.2019.100355 . hal-02447184

HAL Id: hal-02447184

<https://hal.science/hal-02447184>

Submitted on 3 Dec 2020

HAL is a multi-disciplinary open access archive for the deposit and dissemination of scientific research documents, whether they are published or not. The documents may come from teaching and research institutions in France or abroad, or from public or private research centers.

L'archive ouverte pluridisciplinaire **HAL**, est destinée au dépôt et à la diffusion de documents scientifiques de niveau recherche, publiés ou non, émanant des établissements d'enseignement et de recherche français ou étrangers, des laboratoires publics ou privés.

Atomistic Simulations of Basal Dislocations Interacting with Mg₁₇Al₁₂ Precipitates in Mg

Aviral Vaid^a, Julien Guénoles^{b,a,*}, Aruna Prakash^{c,a}, Sandra Korte-Kerzel^b, Erik Bitzek^a

^a*Department of Materials Science and Engineering, Institute I, Friedrich-Alexander-Universität Erlangen-Nürnberg (FAU), Martensstr. 5, 91058 Erlangen, Germany*

^b*Institute of Physical Metallurgy and Metal Physics, RWTH Aachen University, Germany*

^c*Micromechanical Materials Modelling (MiMM), Institute of Mechanics and Fluid Dynamics, Technische Universität Bergakademie Freiberg (TUBAF), Germany*

Abstract

The mechanical properties of Mg-Al alloys are greatly influenced by the complex intermetallic phase Mg₁₇Al₁₂, which is the most dominant precipitate found in this alloy system. The interaction of basal edge and 30° dislocations with Mg₁₇Al₁₂ precipitates is studied by molecular dynamics and statics simulations, varying the inter-precipitate spacing (L), and size (D), shape and orientation of the precipitates. The critical resolved shear stress τ_c to pass an array of precipitates follows the usual $\ln((1/D + 1/L)^{-1})$ proportionality. In all cases but the smallest precipitate, the dislocations pass the obstacles by depositing dislocation segments in the disordered interphase boundary rather than shearing the precipitate or leaving Orowan loops in the matrix around the precipitate. An absorbed dislocation increases the stress necessary for a second dislocation to pass the precipitate also by absorbing dislocation segments into the boundary. Replacing the precipitate with a void of identical size and shape decreases the critical passing stress and work hardening contribution while an artificially impenetrable Mg₁₇Al₁₂ precipitate increases both. These insights will help improve mesoscale models of hardening by incoherent particles.

Keywords: Precipitation Strengthening, Atomistic Simulations, Molecular Dynamics/Statics, Magnesium Alloys, Mg₁₇Al₁₂

1. Introduction

Precipitation strengthening is known to enhance yield and flow stress of metallic alloys by the presence of second-phase particles distributed in a homogenous matrix that impede the motion of dislocations [1]. Various factors are known to influence the strengthening behavior in metallic alloys such as the size, shape, number and distribution of precipitates, the crystallographic alignment between the phases, the interfacial energy and the stacking fault and dislocation energies within the precipitates [2–10].

This strengthening effect is exploited in many engineering alloys, including magnesium. Mg alloys have recently attracted significant interest due to their low density, high specific strength, and good recyclability [11–14]. They are of interest as structural materials for the automotive and aeronautical industries where a strong reduction in components' weight lowers fuel consumption and gas emissions [15]. Understanding the plastic deformation mechanism in such precipitation-strengthened alloys is of prime importance for improving the modeling of light-weight materials and for developing novel alloys with improved prop-

erties. The main alloying element in most Mg alloys is aluminum, which leads to the formation of several intermetallic phases, the most common being Mg₁₇Al₁₂ [11, 16–18]. Mg₁₇Al₁₂, therefore, plays a key role in increasing the yield strength of Mg-Al alloys mainly by hindering the easy glide of dislocations on the basal plane of the Mg-matrix.

The interactions between dislocations and discrete obstacles have been studied since the early days of dislocation theory using experimental techniques [19–23], and linear elasticity [24–26] as well as, more recently, dislocation dynamics modeling [5, 10, 27–30] and atomistic simulations [2, 4, 7–9, 31–36]. A detailed review of atomic-scale modeling of dislocation-obstacle interactions can be found in [3]. Most simulation studies on dislocation-obstacle interactions have so far been performed on fcc and bcc metals. Here, typical obstacles include voids or vacancy clusters and precipitates, either as artificially impenetrable obstacles or by considering realistic material-specific alloy systems. Currently, only comparatively few simulation studies exist in the literature that specifically address dislocation-obstacle interactions in hcp metals, like the recent molecular static simulations by Groh [37] who studied basal edge dislocations in Mg interacting with spherical obstacles generated by artificially immobilizing Mg atoms. Even fewer atomistic simulation studies exist on disloca-

*Corresponding author.

E-mail address: guenole@imm.rwth-aachen.de

tions in simple hcp, fcc or bcc metals interacting with complex intermetallic precipitates [38–40].

Regarding the Mg-Al system of interest in this study, most of the recent work was performed in the group of Horstemeyer[40–42]. However, the properties of the complex intermetallic phase $\text{Mg}_{17}\text{Al}_{12}$ depend crucially on the used interatomic potential. For example, the modified embedded atom model (MEAM) potential by Jelinek *et al.* [43] used by Liao *et al.* [40–42] gives a negative shear modulus C_{44} and a positive enthalpy of formation for the stable $\text{Mg}_{17}\text{Al}_{12}$ phase. More recently, Moitra and Llorca [44] used an embedded atom model (EAM) potential instead of an MEAM potential for the Mg-Al system. However, this potential has a problem with the matrix phase, as EAM potentials, in general, inaccurately represent the elastic constants of hcp materials [45]. For a detailed analysis and comparison of Mg-Al potentials the reader is referred to the supplementary material section S1.

In the following, we present a detailed qualitative as well as quantitative atomistic simulation study of edge and mixed basal dislocations in Mg interacting with different types of obstacles, with the focus on $\text{Mg}_{17}\text{Al}_{12}$ precipitates of varying size, shape and spacing.

2. Methodology

The atomistic simulations presented in this work were performed with the classical molecular dynamics code LAMMPS [46] (version 16 Mar 2018). Atomic interactions were modeled by the MEAM potential of Kim *et al.* [47], which was found to best represent an atomistic system consisting of both Mg and $\text{Mg}_{17}\text{Al}_{12}$ (see supplementary material section S1 for a comparison study between different potentials).

2.1. Sample Setup

A typical simulation setup used in the present work is shown in figure 1. It consists of an hcp-Mg matrix with the basal (0001) plane-normal parallel to the Z-axis, a dislocation with line direction $\xi = [01\bar{1}0]$ parallel to the Y-axis and a precipitate. Periodic boundary conditions (PBC) were used along the dislocation line direction and the direction of dislocation motion, *i.e.*, along the X and Y directions. This setup corresponds therefore to an array of infinite dislocations that interacts with a periodic array of obstacles, as illustrated in fig. 1(b), and allows the study of multiple interactions of the dislocation with the obstacles. Atoms in the top and bottom boundary layers were constricted to move only within the Z-plane (2D dynamic boundary layers).

Edge and 30° dislocations with Burgers vectors $\mathbf{b} = a_0/3 \langle \bar{2}110 \rangle$ were introduced following the method detailed in [48] and [2], where a_0 is the lattice constant of Mg at 0K. The precipitates were inserted approx. 150 Å in front of the dislocation (see fig. 1(b)) by removing the matrix

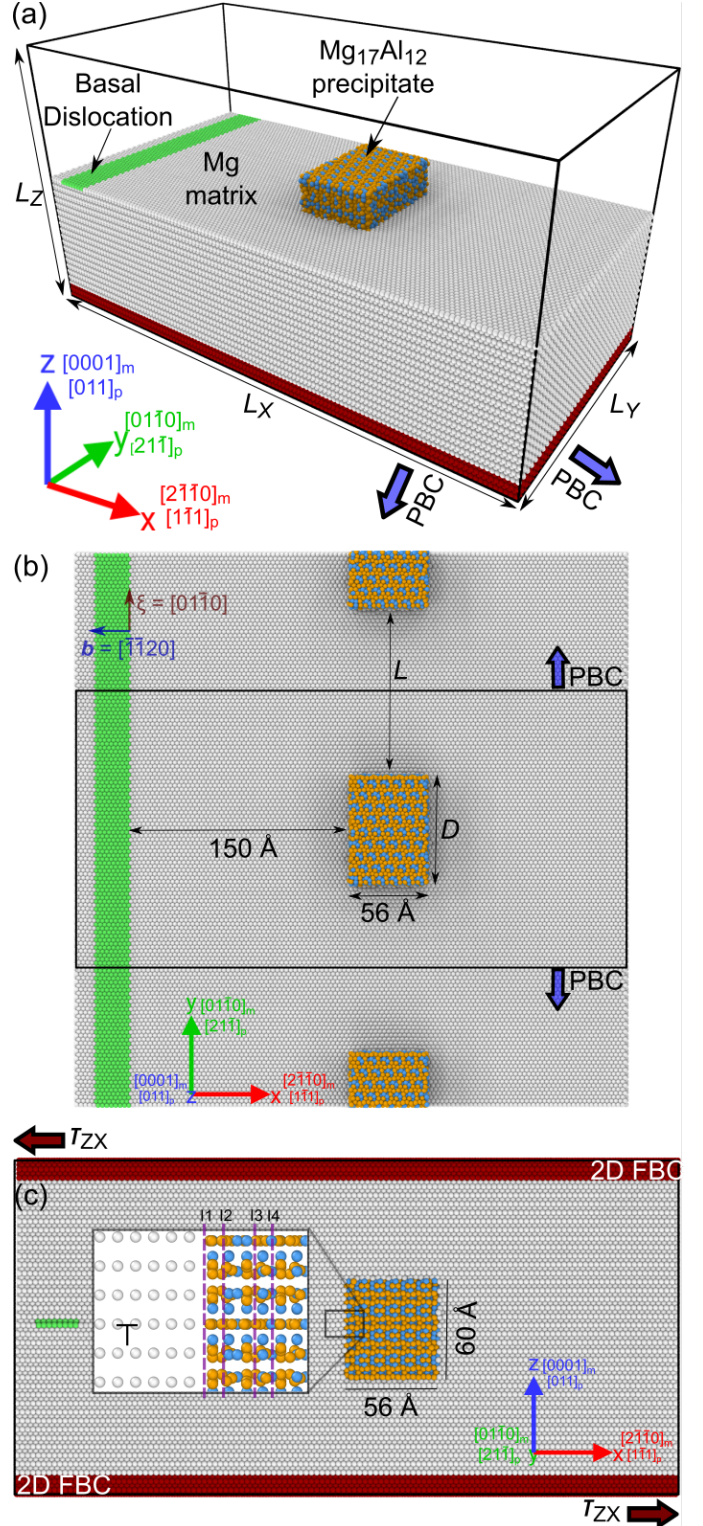


Figure 1: Illustrations of the simulation setup a) perspective and b) top view, with the upper half of Mg atoms removed for clarity. c) side view, cut in the middle of the Y axis. The inset shows the relative alignment of slip plane in Mg to that in $\text{Mg}_{17}\text{Al}_{12}$. The purple lines mark the interface termination (coded as 1, 2, 3, 4). Color code of precipitate atoms based on chemical species: Mg, orange; Al, Blue. Color code of Mg matrix atoms based on local crystallography: fcc, green; hcp, other, grey. Atoms in red are part of the 2D dynamic boundaries. PBC: Periodic boundary conditions, FBC: Force boundary conditions. The simulation box is marked in black.

Table 1: Characteristics of the simulated samples. The samples were varied within a *parameter range* with a *default value* used to build the *default setup*. L denotes the inter-precipitate spacing, \mathbf{b} the Burgers vector and ξ the line direction.

Parameters	Parameter Range	Default setup
<i>Precipitate spacing</i>		
– L (Å)	122, 222, 322, 422, 522	122
<i>Precipitate geometry</i>		
– shape	cuboidal, column, sphere	cuboidal
– width, cuboidal (Å)	78, 156, 234	78
– diameter, sphere (Å)	20, 50, 78	–
<i>Matrix-precipitate interface</i>		
– orientation relationship (OR)	Burgers OR ($L = 122$ Å, $D = 78$ Å), $[1\bar{1}1]_p \parallel [2\bar{1}\bar{1}0]_m$ and $(21\bar{1})_p \parallel (0001)_m$ ($L = 122$ Å, $D = 78$ Å), $[011]_p \parallel [2\bar{1}\bar{1}0]_m$ and $(\bar{1}1\bar{1})_p \parallel (0001)_m$ ($L = 122$ Å, $D = 78$ Å)	Burgers OR
– slip plane alignment	$(0001)_m / (011)_p$, $(0001)_m / (033)_p$	$(0001)_m / (011)_p$
– termination (type)	I1, I2, I3, I4	I1
<i>Dislocation</i>		
– character	edge ($\mathbf{b} = a_0/3 [\bar{2}110]$, $\xi = [01\bar{1}0]$), mixed 30° ($\mathbf{b} = a_0/3 [\bar{1}\bar{1}20]$, $\xi = [01\bar{1}0]$)	edge
<i>Obstacle</i>		
– type	void, precipitate, impenetrable precipitate	precipitate

atoms and filling the resulting void with Mg and Al atoms arranged in the bcc-like crystal structure of the $\text{Mg}_{17}\text{Al}_{12}$ phase (space group $I\bar{4}3m$) [16, 49]. The relative orientation of the Mg matrix and the $\text{Mg}_{17}\text{Al}_{12}$ precipitate follows the experimentally-observed Burgers orientation relationship (OR) [17]: $[1\bar{1}1]_p \parallel [2\bar{1}\bar{1}0]_m$ and $(011)_p \parallel (0001)_m$. The glide plane of the dislocations were aligned with a $\{011\}$ plane in $\text{Mg}_{17}\text{Al}_{12}$, which is assumed to be the natural glide planes of the phase [50, 51], thus presumably allowing for easy slip transmission into the precipitate.

In the present work, we varied the inter-precipitate spacing, precipitate geometry, matrix-precipitate interface, dislocation character and obstacle type ($\text{Mg}_{17}\text{Al}_{12}$ precipitate, $\text{Mg}_{17}\text{Al}_{12}$ precipitate with artificially frozen atoms and a void). Due to the complex crystallography of the precipitate, we prepared various interfaces that follow the Burgers OR while modifying the interface termination at the precipitate (see inset fig. 1(c), supplementary material section S2). The same cuboidal precipitate was additionally rotated by 90° anti-clockwise along X-axis and along Y-axis relative to the position shown in fig. 1(b) to create setups with different interfaces. The variations of the simulation setup are summarized in tab. 1. Most simulations were performed using the values in the last column (tab. 1) and the setup is hereto referred as *default setup*. To study the influence of each parameter, only one characteristic was modified at a time relative to the *default setup* while keeping the others constant. Care was taken to minimize the influence of box size and spurious image forces on the quantitative evaluation of CRSS in our simulations following Szajewski *et al.* [52] (see supplementary material section S3)

2.2. Atomistic Simulations

The created samples were relaxed by first using a local relaxation [53] followed by a full relaxation using an optimized implementation [54] of the FIRE [55] algorithm to reach the equilibrium state. The samples were considered sufficiently relaxed when the force norm, i.e., the norm of the 3N-dimensional force vector, fell below a threshold value of 10^{-8} eV/Å.

The critical resolved shear stress (CRSS) required for a dislocation to overcome the precipitates was computed using a series of molecular statics (MS) simulations. Each setup was pre-sheared along Z in direction of the Burgers vector according to the value of the desired resolved shear stress, using the corresponding elastic constants of the Mg matrix (see supplementary material section S4) Forces corresponding to the desired shear stress were applied to the atoms in the top and bottom layers parallel to the glide plane (2D FBC, see fig 1). This leads to a symmetric shear state on the slip plane situated in the middle of the setup. The CRSS required for a dislocation to overcome a precipitates was determined by bracketing. The *default setup* was also unloaded from a relaxed configuration by removing any externally applied shear stresses and allowing the system to reach an energy minimized state.

The dynamics of the dislocation-obstacle interactions were furthermore studied using molecular dynamics (MD) simulations, using either the NVE ensemble with an initial temperature of $T_0 = 0$ K or in the NVT ensemble at $T = 300$ K (*default setup* with edge or mixed 30° dislocation only). For the 300 K simulations, the sample was expanded according to the lattice constant of the Mg matrix at 300 K and subsequently equilibrated at 300 K for 50 ps while keeping the setup stress-free using Nosé -

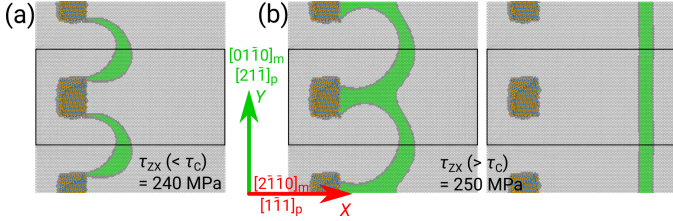


Figure 2: Bracketing of τ_c for the *default setup* ($L = 122 \text{ \AA}$, $D = 78 \text{ \AA}$, edge dislocation). (a) relaxed configuration at $\tau_{zx} (< \tau_c) = 240 \text{ MPa}$. (b) snapshots from the pseudo-dynamics of the relaxation process at $\tau_{zx} (> \tau_c) = 250 \text{ MPa}$.

Hoover thermostat and barostat [56–58]. The time step for all the MD simulations was set to $\delta t = 1.0 \text{ fs}$.

The lower bound of the CRSS corresponds to the highest applied shear stress for which a static simulation (following the above described procedure and minimization criterion) resulted in a stable equilibrium configuration with a pinned dislocation. The upper bound of the CRSS corresponds to the lowest applied shear stress for which no stable equilibrium configuration could be found and the dislocation was no longer pinned. In the following, the CRSS is provided as the central value between the upper and the lower bound while the error gives the interval between these bounds.

2.3. Visualization and Analysis

The Open Visualization Tool (OVITO) [59] was used to visualize and analyze the atomistic configurations. Common neighbor analysis (CNA) [60, 61] was used to identify defects in the Mg matrix. Displacement vector analysis was used to compute the relative displacement between two atomic configurations. Atomic stresses were calculated based on the virial formulation [62] and the atomic Voronoi volume [63, 64]. Stresses represented in the current work have been averaged over the nearest neighbors. Atoms within $\approx 0.5 \text{ nm}$ of the IPB were classified as "other" by the CNA algorithm. Although this classification is often associated to amorphous structures, it is important to point out that the present inter-phase boundary (IPB) structure is not amorphous but rather disordered (see section S5 in the supplementary material).

3. Results

3.1. First dislocation-precipitate interaction

Upon energy minimization, the dislocation in the *default setup* was attracted to the IPB and was found to be already at the precipitate, even when no stress was applied, see fig. S6 in the supplementary material. From this relaxed initial structure, the CRSS for a basal edge dislocation to overcome the precipitate in the *default setup* ($L = 122 \text{ \AA}$, $D = 78 \text{ \AA}$) was determined to be $245 \pm 5 \text{ MPa}$, *i.e.*, at $\tau_{zx} = 240 \text{ MPa}$ minimization resulted in a relaxed pinned dislocation, see fig. 2, whereas at $\tau_{zx} = 250 \text{ MPa}$ the dislocation passed the precipitate array. The relaxed

Table 2: Critical resolved shear stresses τ_c for the studied configurations. Only one parameter is varied at a time, with the others corresponding to the *default setup* (see tab. 1)

Varied parameter	Parameter value	τ_c [MPa]
Precipitate spacing L (\AA)	122	245 ± 5
	222	155 ± 5
	322	115 ± 5
	422	95 ± 5
	522	75 ± 5
<i>Precipitate geometry</i>		
– Cuboidal (width in \AA)	78	115 ± 5
	156	135 ± 5
	234	145 ± 5
– Spherical (diameter in \AA)	20	85 ± 5
	50	195 ± 5
	78	225 ± 5
– Columnar (width in \AA)	78	245 ± 5
<i>Matrix-precipitate interface</i>		
– orientation relationship	Burgers OR	245 ± 5
	$[1\bar{1}1]_p \parallel [2\bar{1}\bar{1}0]_m, (21\bar{1})_p \parallel (0001)_m$	215 ± 5
	$[011]_p \parallel [2\bar{1}\bar{1}0]_m, (\bar{1}1\bar{1})_p \parallel (0001)_m$	215 ± 5
	$(0001)_m / (011)_p$	245 ± 5
– slip plane alignment	$(0001)_m / (033)_p$	245 ± 5
	11 or 13	245 ± 5
– termination (type)	12 or 14	235 ± 5
<i>Dislocation character</i>		
– edge	$(0001)_m / (011)_p$	245 ± 5
	$(0001)_m / (033)_p$	245 ± 5
	$(0001)_m / (011)_p$	275 ± 5
	$(0001)_m / (033)_p$	275 ± 5
Obstacle type	void	195 ± 5
	precipitate	245 ± 5
	frozen atoms	285 ± 5

configuration at $\tau (< \tau_c) = 240 \text{ MPa}$ was furthermore unloaded to 0 stress and a subsequent energy minimization was performed. The parts of the dislocations which were absorbed into the IPB remained in the IPB while the rest of the dislocation line assumed a straight shape, see fig. S9 in the supplementary material. In some setups (depending on dislocation line-length, dislocation character, precipitate shape), the dislocation was not at the interface upon initial energy minimization with $\tau = 0 \text{ MPa}$. These configurations were additionally relaxed with a nominal initial applied stress $\tau = 10 \text{ MPa}$ such that the dislocation was at the matrix-precipitate interface. The CRSS, τ_c , for all simulated configurations in tab. 1 are reported in tab. 2.

Snapshots of the interaction of an initially straight edge dislocation at $\tau_{zx} = 250 \text{ MPa}$ with the precipitates in the *default setup* are shown in fig. 3(a) (NVE, $T_0 = 0 \text{ K}$). At $t = 0 \text{ ps}$, the dislocation started at the leftmost matrix-precipitate interface. The dislocation moved further to the right and at $t = 7 \text{ ps}$ bowed out between the precipitates. At $t = 11 \text{ ps}$, the dislocation reached a maximum bow-out state. The dislocation arms on both sides of the precipitate attracted each other and annihilated at $t = 12 \text{ ps}$, after which the dislocation depinned from the precipitate ($t = 15 \text{ ps}$). Using the common neighbor analysis, no dislocation loops were visible in the matrix around the precipitate, both in the static and in the dynamic simulations at different temperatures.

Figure 4(a) shows the CRSS for different inter-

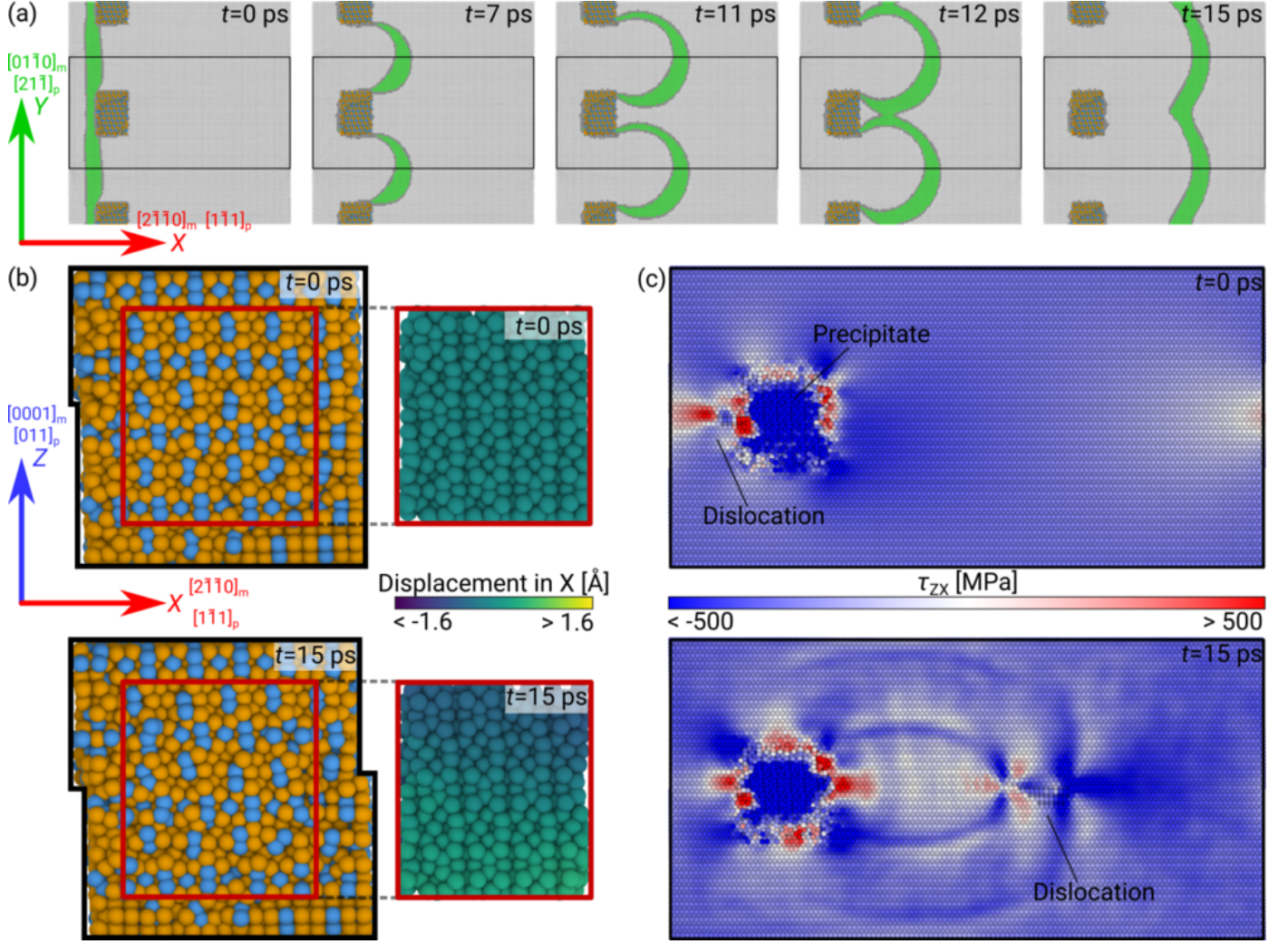


Figure 3: (a) Snapshots of an infinite straight basal edge dislocation interacting with a periodic array of $\text{Mg}_{17}\text{Al}_{12}$ precipitates, as simulated by molecular dynamics (NVE at $T_0 = 0$ K, $\tau_{zx} = 250$ MPa). See fig. 1 for the color coding. (b) $\text{Mg}_{17}\text{Al}_{12}$ precipitate before ($t = 0$ ps) and after ($t = 15$ ps) interaction with an edge dislocation. Please note the step at the matrix-precipitate interface. The insets show the precipitate interior with the color corresponding to the displacement of the atoms along the direction of dislocation motion with respect to the configuration at $t = 0$ ps. (c) stress field τ_{zx} before ($t = 0$ ps) and after ($t = 15$ ps) interaction with an edge dislocation.

precipitate spacings, L . Increasing the inter-precipitate distance resulted in a smaller value of τ_c .

To study the effect of precipitate shape, spherical, rectangle-columnar (spanning the height of the simulation box) and cuboidal (as used for the *default setup*) geometries were used in the simulations. Note that changing the precipitate shape also implies that the matrix-precipitate interfaces were crystallographically different. The CRSS for a spherical precipitate was lower than for cuboidal or columnar precipitates (see fig. 4(b), $L = 122$ Å). The mechanism by which the dislocation passes the precipitates was the same for all precipitates, except for the spherical one with a diameter of 20 Å, which was cut by the incoming dislocation.

Figure 4(b) also shows the effect of varying precipitate size (width for cuboidal, diameter for spherical precipitates) on τ_c . Instead of the default value of $L = 122$ Å a larger value of $L = 322$ Å was constantly used for a

cuboidal precipitate. As can be seen in fig. 4(b) the CRSS showed a logarithmical dependence with the precipitate size.

To study the influence of the matrix-precipitate interface structure on the dislocation-precipitate interaction, the interface was modified in three ways: (1) by rotating the precipitate and thus, changing the orientation relationship between the matrix and the precipitate, (see tab. 2) (2) by changing the slip plane of the matrix dislocation so that it aligns with the $\{330\}$ plane of the $\text{Mg}_{17}\text{Al}_{12}$ precipitate instead of the $\{110\}$ plane, and (3) by changing the termination plane of the precipitate at the matrix-precipitate interface (see supplementary material section S2). Changing the OR between the matrix and precipitate may change the effective inter-precipitate distance and the precipitate width, leading to a lower CRSS. Changing the relative alignment of the slip plane of the matrix dislocation with respect to the precipitate did not influence the

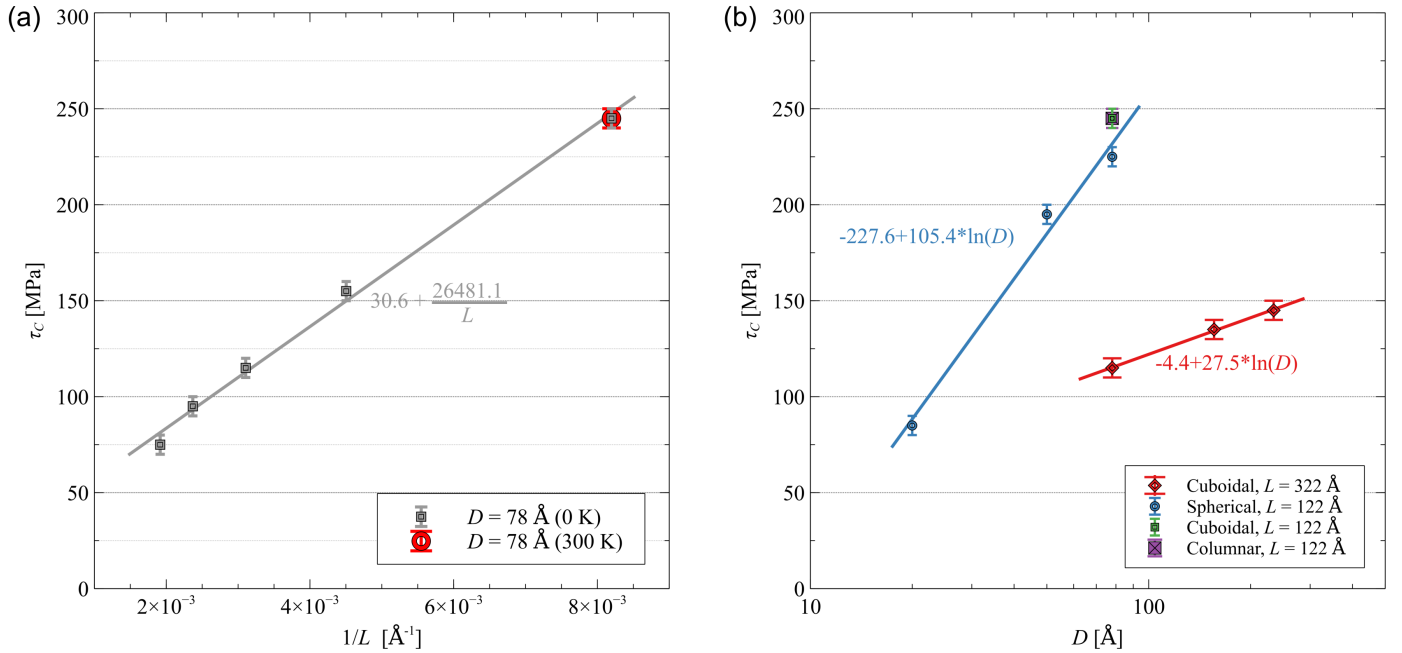


Figure 4: Dependence of the critical resolved shear stress (CRSS) on (a) inter-precipitate spacing L and (b) precipitate size.

CRSS. Changing the termination plane of the precipitate at the matrix-precipitate resulted in only slight variations in τ_c as can be seen in tab. 2.

To study the influence of the character of the dislocation on its interaction with the precipitate, a 30° dislocation was introduced in the matrix instead of the default edge dislocation. Forces equivalent to a shear stress greater than τ_c were applied to the system along the direction of the Burgers vector. Figure 5 shows the interaction of a 30° dislocation with $\text{Mg}_{17}\text{Al}_{12}$ precipitates in an NVE simulation at 0 K. The shown stages of dislocation-precipitate interactions are the same as in fig. 3(a), however, as the dislocation did not approach the precipitate during energy minimization, the times in both figures are not identical. At $t = 8$ ps, the dislocation arrived at the matrix-precipitate interface, and continued to move along the sides of the precipitates (see $t = 14$ ps). At $t = 15$ ps, the dislocation reached its maximum bow out state. Before overcoming the precipitate, the dislocation arms interacted and annihilated each other ($t = 16$ ps) before the dislocation finally detached ($t = 21$ ps). In contrast to the edge dislocation, fig. 3(a), the maximum bow-out configuration of the 30° dislocation was asymmetric, but the overall mechanism of interaction was similar to the edge dislocation case. The CRSS for the 30° dislocation was about 10% larger than that for an edge dislocation (see tab. 2). Similar to the edge dislocation case, changing the alignment of the slip plane did not affect the CRSS.

We performed additional simulations of selected configurations at 300 K and found no change of interaction mechanism for either edge or 30° dislocations (see supplementary material section S6), and the CRSS of the *default setup* was - within the bracketing interval - identical to the

CRSS at 0 K (see figure 4).

Two extreme cases of obstacles were studied in addition to the default $\text{Mg}_{17}\text{Al}_{12}$ precipitate: an impenetrable $\text{Mg}_{17}\text{Al}_{12}$ precipitate achieved by fixing the corresponding atomic positions, and a void, both of the same shape and size as the default precipitate. Figure 6 shows snapshots from the corresponding MD simulations (NVE, $T_0 = 0$ K) when the edge dislocation has passed the obstacle. In the case of the void, fig. 6(a), the dislocation was attracted to the void. The part of the dislocation touching the void disappeared at the free surface leaving a step, while the remaining dislocation moved along the void, bowed out with the side arms annihilating and creating a step at the back surface of the void in the process. With the fixed $\text{Mg}_{17}\text{Al}_{12}$ precipitate (fig. 6(c)), the dislocation overcame the precipitate by Orowan looping, similar to the already addressed case of the default $\text{Mg}_{17}\text{Al}_{12}$ precipitate fig. 6(b). In this case, a dislocation loop in the matrix was clearly detected by the CNA algorithm. The corresponding stress states after obstacle passage are also shown on the right of fig. 6.

The CRSS to pass the void was 20% lower than for the $\text{Mg}_{17}\text{Al}_{12}$ precipitate of identical size. The impenetrable $\text{Mg}_{17}\text{Al}_{12}$ precipitate, on the other hand, required an about 15% higher resolved shear stress than the $\text{Mg}_{17}\text{Al}_{12}$ precipitate with mobile atoms, see fig. 6(d).

3.2. Second dislocation-precipitate interaction

After having overcome the obstacle, the dislocation can pass through the PBC and interact a second time with the same obstacle. Quasi-static simulations were performed iteratively by increasing the applied shear stress by 10 MPa until the dislocation overcame the obstacle during

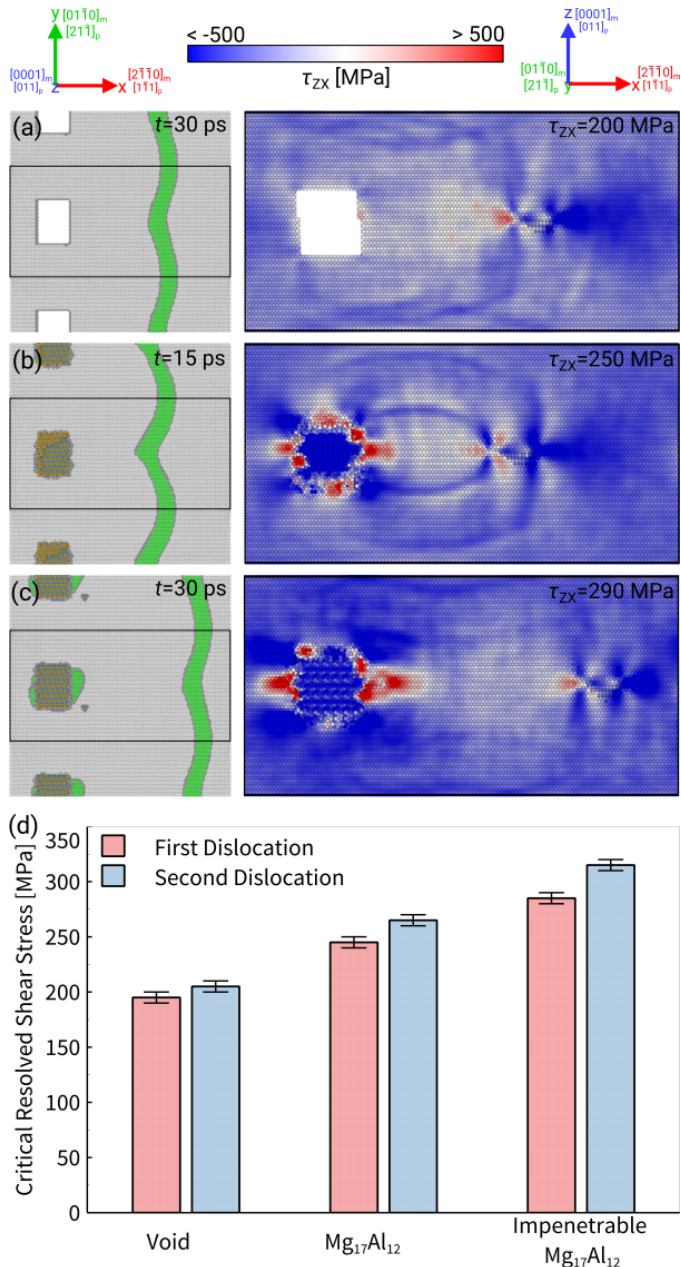


Figure 6: Top view of the setup (left) and side view of the stress field τ_{zx} (right) after a dislocation has overcome an array of (a) voids, (b) $\text{Mg}_{17}\text{Al}_{12}$ precipitates, and (c) impenetrable $\text{Mg}_{17}\text{Al}_{12}$ precipitates the first time studied using NVE at $T_0 = 0$ K ($L = 122$ Å, $D = 78$ Å). (d) Variation in critical resolved shear stress with modification of obstacle type.

dislocation would have been effectively *climbing* over the precipitate. The way the IPBs are created in the atomistic simulations can therefore have important consequences on the dislocation precipitate interaction mechanisms.

High-resolution transmission electron microscopy (HR-TEM) analysis of Mg- $\text{Mg}_{17}\text{Al}_{12}$ interfaces shows local distortions at the interphase boundary [70, 71]. Although, these images may not directly resolve the local structure, the loss of contrast from distinct atomic columns indicates that the interface is not perfectly coherent despite the ori-

entation relationship being maintained between the two phases. This observation agrees with the disordered IPB structure in our simulations (see supplementary material section S5) An IPB with excess free volume (see also fig. S4 in the supplementary material) facilitates the absorption of dislocations. The IPB thickness of approx. 0.5 nm surrounding the particle in our simulations also explains why the smallest 2 nm spherical precipitate was sheared in our simulations, as nearly most of its atoms were part of the IPB.

In order for dislocations to be absorbed in the Mg/ $\text{Mg}_{17}\text{Al}_{12}$ IPB, the image force on the dislocation caused by the different elastic constants of the precipitate and the matrix [72] has to be either negligible or attractive. A repulsive image force as in the case of the fixed $\text{Mg}_{17}\text{Al}_{12}$ would cause a certain stand-off distance of the dislocation, resulting in a visible Orowan loop as can be seen in fig. 6(c). Using the shear modulus in slip plane and slip direction with the values for the used potential shows that $\mu'(\text{Mg}) = 17.2$ GPa $\approx \mu'(\text{Mg}_{17}\text{Al}_{12}) = 17.6$ GPa (see supplementary material section S4). Comparing the elastic constants from MEAM potential with DFT and experiments for both phases, no differences are expected (supplementary material section S1).

From the fact that the precipitate in the *default setup* is not sheared by a second dislocation, one can deduce a lower bound for the CRSS to shear the $\text{Mg}_{17}\text{Al}_{12}$ by assuming a pile-up of $n = 2$ dislocations at an applied shear stress of $\tau = 250$ MPa, fig. 6(d), to $\tau_{c,\min} = n\tau = 500$ MPa. This is consistent with the higher stress required to move dislocations in the complex intermetallic phase $\text{Mg}_{17}\text{Al}_{12}$ compared with the pure metallic Mg matrix. At room temperature, the hardness of $\text{Mg}_{17}\text{Al}_{12}$ has been measured as 2 GPa and 3.5 GPa in micro- and nano-hardness measurements, respectively [73, 74]. In contrast, the micro-hardness of pure magnesium has been measured to 0.34 GPa [75]. The much higher hardness of the intermetallic phase is also evidenced by its brittle behavior at room temperature, where fracture becomes dominant in macroscopic mechanical testing [51, 76–78]. This is consistent with the tetrahedral packing leading to corrugated crystallographic planes in $\text{Mg}_{17}\text{Al}_{12}$ and the correspondingly large perfect Burgers vector expected on these planes which lead to limited thermal activation of dislocation glide, as found in hardness measurements between room temperature and $0.54 T_m$ [73]. Although Xiao *et al.* [50] suggested a specific (110) slip plane and microcompression experiments have confirmed slip traces consistent with this type of plane [79], the actual Burgers vector, including that of any partial dislocations and the exact slip planes of $\text{Mg}_{17}\text{Al}_{12}$ have, however, not yet been unambiguously identified.

The critical resolved shear stress in dislocation - obstacle interactions can be significantly reduced by so called 'inertial overshooting', particular at low temperatures and high dislocation velocities [2, 55]. As FIRE uses 0K pseudo-

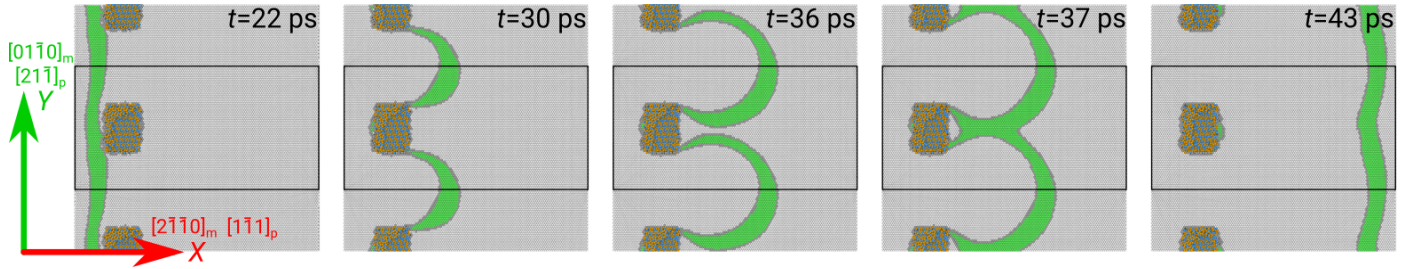


Figure 7: Snapshots of a second infinite straight basal edge dislocation interacting with a periodic array of $\text{Mg}_{17}\text{Al}_{12}$ precipitates for the default setup (NVE at $T_0 = 0$ K, $\tau_{zx} = 270$ MPa). See fig. 1 for the color coding.

dynamics [55], similar inertial effects can in principle occur during minimization if the dislocations are initially far away from the obstacles. In the present study, however, no such inertial effects are expected as the dislocations were close to the precipitates when the CRSS was determined.

The critical resolved shear stress τ_c to unpinned a dislocation from a periodic array of strong obstacles like voids or impenetrable particles has been shown to be dominated by the stress necessary to pull out the dislocation segments at the obstacle into a parallel dipole [80]. Bacon, Kocks and Scattergood [80] and Scattergood and Bacon [81] developed the following expression for τ_c by fitting their results obtained by computer simulations based on elasticity theory, which explicitly modeled the self-stress of a flexible dislocation:

$$\tau_c = \frac{\mu' b}{2\pi AL} \left(\ln(\bar{D}) + \Delta \right). \quad (1)$$

In this expression, which will henceforth be referred to as the BKS model, μ' is the shear modulus in slip plane and slip direction, A equals 1 for an initially pure edge dislocation and $(1-\nu)$ for a pure screw dislocation, where ν is Poisson's ratio, b is the magnitude of the Burgers vector and \bar{D} is the harmonic mean of the inter-obstacle spacing L and the obstacle width D : $\bar{D} = (b/L + b/D)^{-1}$. The empirical constant Δ models the energetic costs associated with the specific dislocation-obstacle interaction. In the case of a void, it describes the resisting force caused by creation of a surface step [81]:

$$\Delta = \frac{\delta\gamma}{\frac{\mu' b}{4\pi} \ln(R/r_0)}. \quad (2)$$

Here, $\delta\gamma$ is the energy of the newly created interface (in case of a void, $\delta\gamma$ equals γ_{surf} , the energy of a free surface) and R, r_0 are the outer and inner cut-off radii in the calculation of dislocation energy (the factor $\ln(R/r_0)$ is usually taken to be unity).

Figure 8 shows the values of τ_c determined from the simulations of an edge dislocation interacting with $\text{Mg}_{17}\text{Al}_{12}$ precipitates of various diameters and spacing as function of \bar{D} . Using the BKS model with $\mu' = 17.2$ GPa, $b = 3.204$ Å and an estimate for the interface step energy $\delta\gamma = \gamma_{\text{interface}} = 309$ mJ m^{-2} calculated for a $(011)_p$ $\parallel (0001)_m$ interface (following the same methodology as

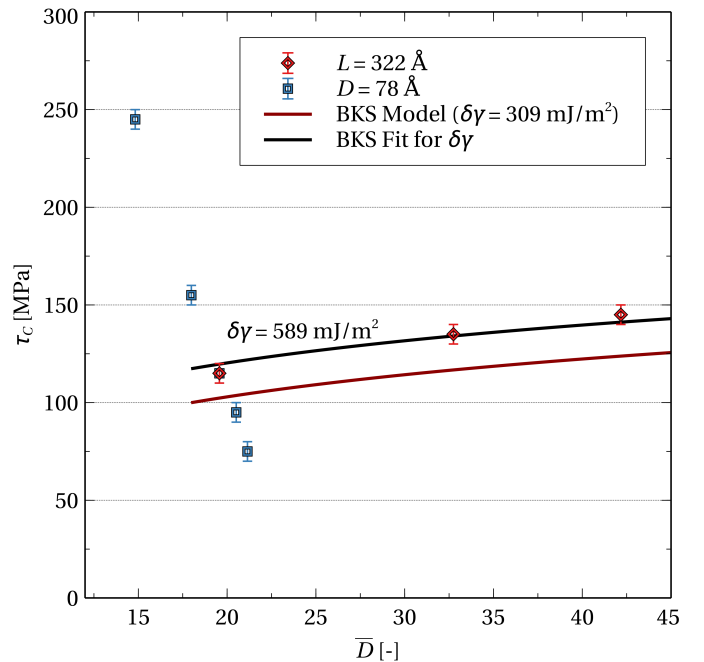


Figure 8: Critical resolved shear stress τ_c for an edge dislocation to pass $\text{Mg}_{17}\text{Al}_{12}$ precipitates with a constant spacing L and varying diameter D , as well as constant D and varying L plotted against the harmonic mean, \bar{D} . Atomistic simulations (data points), BKS model using $\delta\gamma = \gamma_{\text{interface}}$ (red line) and with fitted $\delta\gamma$ (black line).

in [82]) results in too low values for τ_c compared to the simulations. Fitting the BKS model to the data results in $\delta\gamma = 589$ mJ m^{-2} , i.e., the energy of the absorbed dislocation in the IPB is much larger than the energy created by interfacial steps of width b .

The energy of the absorbed dislocation in the IPB, modeled by Δ in eq. 1, can be influenced by the temperature. In the simulations, no effect of temperature was observed on the CRSS at 300K (see figure 4) for $L = 122$ Å, $D = 78$ Å, $\bar{D} = 14.83$. On experimental time scales the dislocation core might spread and dissolve within the IPB, which could lead to some temperature dependence of the CRSS. The main contribution to the obstacle strength is however the elastic energy due to the dislocation dipole configuration, which should not be strongly dependent on temperature.

Interestingly, the BKS model predicts a larger τ_c

for voids than for the Orowan process ($\Delta(\text{Orowan}) = 0.77, \Delta(\text{void}) = 1.52$ [80, 81]). Our simulations with $D = 78 \text{ \AA}$ and $L = 122 \text{ \AA}$ ($\bar{D} = 14.83$), however, show that the void has ≈ 0.8 times smaller τ_c than an $\text{Mg}_{17}\text{Al}_{12}$ precipitate with identical D and L , see fig. 6(d). This points to the importance of the specific details of the precipitate and the IPB, which were not accounted for in the derivation of the BKS model [80] and can become particularly important for small \bar{D} .

This becomes particularly evident when considering the fixed $\text{Mg}_{17}\text{Al}_{12}$ precipitate, which has a ≈ 1.2 times higher τ_c than the $\text{Mg}_{17}\text{Al}_{12}$ precipitate. Here, the infinitely stiff obstacle leads to high image forces and subsequently a higher energy of the Orowan loop, which are not accounted for in the original BKS model with non-interacting obstacles of identical elastic properties as the matrix [80]. Their model of a flexible dislocation, however, captures the importance of the Burgers vector orientation relative to the obstacle row and predicts a higher τ_c for mixed dislocations as compared to a pure edge dislocation, in agreement with our results for a 30° dislocation, see tab. 2.

The BKS model does not consider the interaction of multiple dislocations with the same obstacle, i.e., the change of τ_c upon repeated bowing or cutting, which would reflect as hardening or softening during ongoing plastic deformation. In agreement with the simulation results on voids, fig. 6(d), no significant change in τ_c is expected for voids that are not completely sheared apart, as the increase in surface energy γ_{surf} is not expected to change much with the step size. For the Orowan process, however, the Orowan loops left around the obstacle by previously interacting dislocations affect subsequent dislocations. I.e., the work hardening rate for metals and alloys containing unsharable particles is different from the same material without particles or with shearable precipitates [25, 29, 83]. The Orowan loops contribute to short- and long-range interactions with other dislocations [83]. The short-range interaction reduces the effective inter-particle distance and has a significant strengthening effect. This so-called source-shortening effect [25] was recently studied by dislocation dynamics simulations, where Queyreau *et al.*[29] could show that this effect of the accumulated Orowan loops can indeed be modeled by the classical approach of assuming an increased effective particle diameter $D_{\text{II}} > D_{\text{I}}$ and correspondingly a smaller L_{II} in Eq. 1 [84], as illustrated in fig. 9(a).

The dislocation absorbed in the IPB clearly affects the second dislocation and leads to an increase in τ_c for the following dislocation, see figs. 6(d) and 7. However, due to the absorption in the IPB, the effective particle diameter will not be the same as in the case of an Orowan loop in the matrix, even for otherwise identical particles. Furthermore, the line energy and stress field of dislocations can change upon absorption [68, 69, 86, 87], see also the stress fields in figs. 6(b) vs. 6(c). The contribution to work hardening by precipitates with absorbing interfaces is therefore expected to be different than for particles with interfaces that can-

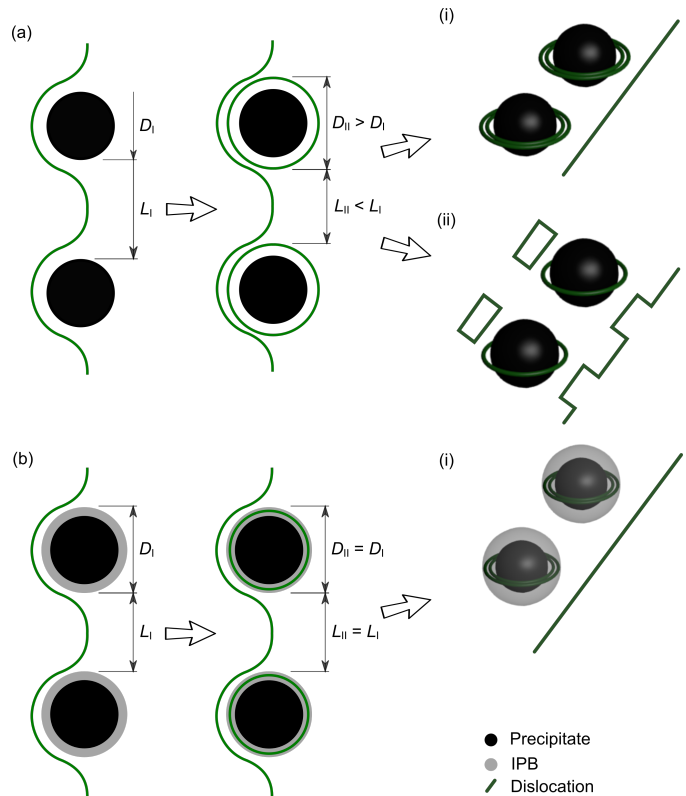


Figure 9: Schematics of the mechanisms of an edge dislocation interacting with impenetrable obstacles: (a) Orowan mechanism (after [85]), leading to one or multiple loops in the matrix around the precipitate (i), combined cross-slip-Orowan mechanism according to Hirsch [19, 20] (ii); (b) possible interaction mechanisms when the dislocation is absorbed in the IPB. (Effective) inter-precipitate spacing L_{I} (L_{II}) experienced during the first (second) dislocation-precipitate interaction and (effective) precipitate diameter D_{I} (D_{II}) experienced during the first (second) dislocation-precipitate interaction.

not absorb dislocations, even if other particle properties remain identical. Changes of dislocation properties in interfaces were first considered in the case of diffusive processes [86, 88, 89], where it helped to explain the creep behavior of oxide-dispersion strengthened (ODS) superalloys. The recent observations of dislocation-precipitate interactions by Huang *et al.*[87], however, suggest that diffusion-less interfacial dislocation relaxation processes can lower the line energy of dislocations absorbed in an IPB.

A further consequence of dislocations being absorbed in particle interfaces is that in contrast to Orowan loops in the matrix, they cannot take part in cross-slip processes. The combined cross-slip, Orowan mechanisms as suggested by Hirsch [19, 20], see also fig. 9(a)(ii), can therefore not take place. Figure 9 summarizes the different mechanisms possible in the case of Orowan looping in the matrix and dislocation absorption into the IPB.

In the present simulations, only dislocations in Mg interacting with $\text{Mg}_{17}\text{Al}_{12}$ precipitates were shown to be absorbed into the IPB. However, the recent in-situ TEM indentation experiments on Mg-Nd alloys by Huang *et al.*[87] showed dislocation absorption at the interface of β_1 pre-

precipitates of the DO_3 structure. Dislocation absorption into precipitate IPBs might therefore be more common for incoherent particles. The implications, like changes in dislocation energy and stress field, and unavailability of dislocations for cross-slip processes, are, however, to our knowledge not yet included in mesoscale models of particle hardening.

5. Summary

Molecular statics and dynamics simulations were performed on basal edge and 30° dislocations in Mg interacting with an array of $\text{Mg}_{17}\text{Al}_{12}$ precipitates to determine the critical stress for obstacle passing and study the mechanisms of dislocation-precipitate interactions. Independent of temperature (up to 300 K), precipitate diameter ($20 \text{ \AA} < D < 235 \text{ \AA}$), precipitate shape, precipitate orientation, precipitate spacing, dislocation type, the relative alignment of slip planes in matrix and precipitate, and the preparation of the matrix-precipitate interface, the dislocations leave no visible Orowan loop in the matrix around the precipitate. Although a step is visible at the matrix-precipitate interphase boundary, the precipitate is not sheared, but the dislocation forming the Orowan loop is absorbed into the disordered boundary. As expected for Orowan looping, the critical resolved shear stress to pass the precipitates is not significantly influenced by changes in the matrix-precipitate orientation relationship or precipitate shape, as well as temperature, and is well-described by the Bacon, Kocks and Scattergood model. However, changing the type of obstacle by either removing all atoms belonging to the $\text{Mg}_{17}\text{Al}_{12}$ precipitate and creating a void, or by fixing all their atomic positions and creating a stiff impenetrable obstacle changes the obstacle strength as well as the stress necessary for a second dislocation to pass the obstacles. The observed absorption of dislocations into the precipitate-matrix interface has important consequences for particle hardening, as this influences the dislocation line energy and stress field, and the absorbed Orowan loops are not available for subsequent combined cross-slip Orowan mechanisms. Inclusion of these effects might be important for quantitative mesoscale models of particle hardening.

Acknowledgements

The authors acknowledge financial support by the Deutsche Forschungsgemeinschaft (DFG) within the Cluster of Excellence “Engineering of Advanced Materials” (Project EXC 315, including Bridge Funding). AV thanks Peter Felfer for his help with the figures. Computing resources were provided by the Regionales RechenZentrum Erlangen (RRZE)

References

[1] E. Nembach, Particle strengthening of metals and alloys, A Wiley-Interscience publication, J. Wiley, 1997.

[2] E. Bitzek, P. Gumbsch, Dynamic aspects of dislocation motion: Atomistic simulations, *Materials Science and Engineering A* 400-401 (1-2 SUPPL.) (2005) 40–44. doi:10.1016/j.msea.2005.03.047.

[3] D. J. Bacon, Y. N. Osetsky, D. Rodney, Chapter 88 Dislocation–Obstacle Interactions at the Atomic Level, in: J. P. Hirth, L. B. T. D. i. S. Kubin (Eds.), *Dislocations in Solids*, Vol. 15, Elsevier, 2009, pp. 1–90. arXiv:arXiv:1011.1669v3, doi:https://doi.org/10.1016/S1572-4859(09)01501-0.

[4] Y. Osetsky, D. Bacon, Void and precipitate strengthening in α -iron: what can we learn from atomic-level modelling?, *Journal of Nuclear Materials* 323 (2-3) (2003) 268–280. doi:10.1016/j.jnucmat.2003.08.028.

[5] C. S. Shin, M. C. Fivel, M. Verdier, K. H. Oh, Dislocation-impenetrable precipitate interaction: A three-dimensional discrete dislocation dynamics analysis, *Philosophical Magazine* 83 (31-34) (2003) 3691–3704. doi:10.1080/14786430310001599379.

[6] A. Takahashi, N. Ghoneim, A computational method for dislocation–precipitate interaction, *Journal of the Mechanics and Physics of Solids* 56 (4) (2008) 1534–1553. doi:10.1016/j.jmps.2007.08.002.

[7] C. Kohler, P. Kizler, S. Schmauder, Atomistic simulation of precipitation hardening in α -iron: Influence of precipitate shape and chemical composition, *Modelling and Simulation in Materials Science and Engineering* 13 (1) (2005) 35–45. doi:10.1088/0965-0393/13/1/003.

[8] D. A. Terentyev, G. Bonny, L. Malerba, Strengthening due to coherent Cr precipitates in Fe-Cr alloys: Atomistic simulations and theoretical models, *Acta Materialia* 56 (13) (2008) 3229–3235. doi:10.1016/j.actamat.2008.03.004.

[9] D. Terentyev, L. Malerba, Interaction of a screw dislocation with Cu-precipitates, nanovoids and Cu-vacancy clusters in BCC iron, *Journal of Nuclear Materials* 421 (1-3) (2012) 32–38. doi:10.1016/j.jnucmat.2011.11.037.

[10] a. Takahashi, K. Kurata, Dislocation dynamics based modelling of dislocation-precipitate interactions in bcc metals, *IOP Conference Series: Materials Science and Engineering* 10 (2010) 012081. doi:10.1088/1757-899X/10/1/012081.

[11] I. J. Polmear, Magnesium alloys and applications, *Materials Science and Technology* 10 (1) (1994) 1–16. doi:10.1179/mst.1994.10.1.1.

[12] A. Luo, M. O. Pekguleryuz, Cast magnesium alloys for elevated temperature applications, *Journal of Materials Science* 29 (20) (1999) 5259–5271. doi:10.1007/BF01171534.

[13] G. Hanko, H. Antrekowitsch, P. Ebner, Recycling automotive magnesium scrap, *Jom* 54 (2) (2002) 51–54. doi:10.1007/BF02701075.

[14] J. Bohlen, D. Letzig, K. U. Kainer, New perspectives for wrought magnesium alloys, in: *Materials science forum*, Vol. 546, Trans Tech Publ, 2007, pp. 1–10.

[15] M. Bamberger, G. Dehm, Trends in the Development of New Mg Alloys, *Annual Review of Materials Research* 38 (1) (2008) 505–533. doi:10.1146/annurev.matsci.020408.133717.

[16] N. Wang, W.-Y. Yu, B.-Y. Tang, L.-M. Peng, W.-J. Ding, Structural and mechanical properties of $\text{Mg}_{17}\text{Al}_{12}$ and Mg_{24}Y_5 from first-principles calculations, *Journal of Physics D: Applied Physics* 41 (19) (2008) 195408. doi:10.1088/0022-3727/41/19/195408.

[17] J. Clark, Age hardening in a Mg-9 wt.% Al alloy, *Acta Metallurgica* 16 (2) (1968) 141–152. doi:10.1016/0001-6160(68)90109-0.

[18] J. Bursšik, M. Svoboda, A HREM and Analytical STEM Study of Precipitates in an AZ91 Magnesium Alloy, *Microchimica Acta* 139 (1-4) (2002) 39–42. doi:10.1007/s006040200036.

[19] F. Humphreys, P. B. Hirsch, The deformation of single crystals of copper and copper-zinc alloys containing alumina particles-ii. microstructure and dislocation-particle interactions, *Proc. R. Soc. Lond. A* 318 (1532) (1970) 73–92.

[20] P. B. Hirsch, The interpretation of the slip pattern in terms of dislocation movements, *J. Inst. Met* 86 (13) (1957) 1958.

- [21] F. Delmas, M. Vivas, P. Lours, M. J. Casanove, A. Couret, A. Coujou, Straining mechanisms in aluminium alloy 6056. In-situ investigation by transmission electron microscopy, *Materials Science and Engineering A* 340 (1-2) (2003) 286–291. doi:10.1016/S0921-5093(02)00184-3.
- [22] G. Liu, I. Robertson, Three-dimensional visualization of dislocation-precipitate interactions in a Al–4Mg–0.3Sc alloy using weak-beam dark-field electron tomography, *Journal of Materials Research* 26 (04) (2011) 514–522. doi:10.1557/jmr.2010.83.
- [23] J. Takahashi, K. Kawakami, Y. Kobayashi, Consideration of particle-strengthening mechanism of copper-precipitation-strengthened steels by atom probe tomography analysis, *Materials Science and Engineering A* 535 (2012) 144–152. doi:10.1016/j.msea.2011.12.056.
- [24] E. Nembach, Precipitation hardening caused by a difference in shear modulus between particle and matrix, *physica status solidi (a)* 78 (2) (1983) 571–581. doi:10.1002/pssa.2210780223.
- [25] L. M. Brown, W. M. Stobbs, The work-hardening of copper-silica i. A model based on internal stresses, with no plastic relaxation, *Philosophical Magazine* 23 (185) (1971) 1201–1233. doi:10.1080/14786437108217406.
- [26] P. M. Hazzledine, P. B. Hirsch, A coplanar Orowan loops model for dispersion hardening, *Philosophical Magazine* 30 (6) (1974) 1331–1351. doi:10.1080/14786437408207286.
- [27] G. Monnet, S. Naamane, B. Devincere, Orowan strengthening at low temperatures in bcc materials studied by dislocation dynamics simulations, *Acta Materialia* 59 (2) (2011) 451–461. doi:10.1016/j.actamat.2010.09.039.
- [28] Y. Xiang, D. J. Srolovitz, L. T. Cheng, W. E. Level set simulations of dislocation-particle bypass mechanisms, *Acta Materialia* 52 (7) (2004) 1745–1760. doi:10.1016/j.actamat.2003.12.016.
- [29] S. Queyreau, G. Monnet, B. Devincere, Orowan strengthening and forest hardening superposition examined by dislocation dynamics simulations, *Acta Materialia* 58 (17) (2010) 5586–5595. arXiv:1106.3789, doi:10.1016/j.actamat.2010.06.028.
- [30] Y. Xiang, D. J. Srolovitz, Dislocation climb effects on particle bypass mechanisms, *Philosophical Magazine* 86 (25-26) (2006) 3937–3957. doi:10.1080/14786430600575427.
- [31] T. Hatano, Dynamics of a dislocation bypassing an impenetrable precipitate: The Hirsch mechanism revisited, *Physical Review B - Condensed Matter and Materials Physics* 74 (2) (2006) 1–4. arXiv:0511358v2, doi:10.1103/PhysRevB.74.020102.
- [32] A. Takahashi, Y. Aoki, M. Kikuchi, Molecular dynamics simulation of interaction between screw dislocation and copper precipitate in iron, *Adv. Mater. Res.* 33 (112) (2008) 895–900. doi:10.4028/www.scientific.net/AMR.33-37.895.
- [33] D. J. Bacon, Y. N. Osetsky, Mechanisms of hardening due to copper precipitates in α -iron, *Philosophical Magazine* 89 (34-36) (2009) 3333–3349. doi:10.1080/14786430903271377.
- [34] L. Proville, B. Bakó, Dislocation depinning from ordered nanophases in a model fcc crystal: From cutting mechanism to Orowan looping, *Acta Materialia* 58 (17) (2010) 5565–5571. doi:10.1016/j.actamat.2010.06.018.
- [35] D. Terentyev, L. Malerba, G. Bonny, A. T. Al-Motasem, M. Poselt, Interaction of an edge dislocation with Cu-Ni-vacancy clusters in bcc iron, *Journal of Nuclear Materials* 419 (1-3) (2011) 134–139. doi:10.1016/j.jnucmat.2011.08.021.
- [36] A. Prakash, J. Guérolé, J. Wang, J. Müller, E. Spiecker, M. Mills, I. Povstugar, P. Choi, D. Raabe, E. Bitzek, Atom probe informed simulations of dislocation-precipitate interactions reveal the importance of local interface curvature, *Acta Materialia* 92 (0) (2015) 33–45. doi:10.1016/j.actamat.2015.03.050.
- [37] S. Groh, Transformation of shear loop into prismatic loops during bypass of an array of impenetrable particles by edge dislocations, *Materials Science and Engineering A* 618 (2014) 29–36. doi:10.1016/j.msea.2014.08.079.
- [38] H. Fan, Y. Zhu, Q. Wang, Effect of precipitate orientation on the twinning deformation in magnesium alloys, *Computational Materials Science* 155 (2018) 378–382.
- [39] H. Fan, Y. Zhu, J. A. El-Awady, D. Raabe, Precipitation hardening effects on extension twinning in magnesium alloys, *International Journal of Plasticity* 106 (2018) 186–202.
- [40] M. Liao, B. Li, M. F. Horstemeyer, Interaction Between Basal Slip and a $Mg_{17}Al_{12}$ Precipitate in Magnesium, *Metallurgical and Materials Transactions A* 45 (8) (2014) 3661–3669. doi:10.1007/s11661-014-2284-3.
- [41] M. Liao, B. Li, M. F. Horstemeyer, Interaction between prismatic slip and a $Mg_{17}Al_{12}$ precipitate in magnesium, *Computational Materials Science* 79 (2013) 534–539. doi:10.1016/j.commatsci.2013.07.016.
- [42] M. Liao, B. Li, M. F. Horstemeyer, Unstable dissociation of a prismatic dislocation in magnesium, *Scripta Materialia* 69 (3) (2013) 246–249. doi:10.1016/j.scriptamat.2013.04.008.
- [43] B. Jelinek, S. Groh, M. F. Horstemeyer, J. Houze, S. G. Kim, G. J. Wagner, A. Moitra, M. I. Baskes, Modified embedded atom method potential for Al, Si, Mg, Cu, and Fe alloys, *Physical Review B - Condensed Matter and Materials Physics* 85 (24). doi:10.1103/PhysRevB.85.245102.
- [44] A. Moitra, J. LLorca, Atomistic simulations of dislocation/precipitation interactions in Mg-Al alloys and implications for precipitation hardening, *ArXiv e-prints* arXiv:1704.03487.
- [45] R. Pasianot, E. J. Savino, Embedded-atom-method interatomic potentials for hcp metals, *Physical Review B* 45 (22) (1992) 12704–12710. doi:10.1103/PhysRevB.45.12704.
- [46] S. Plimpton, Fast parallel algorithms for short-range molecular dynamics, *Journal of Computational Physics* 117 (1995) 1–19. doi:10.1006/jcph.1995.1039.
- [47] Y.-M. M. Kim, N. J. Kim, B.-J. J. Lee, Atomistic Modeling of pure Mg and Mg-Al systems, *Calphad* 33 (4) (2009) 650–657. doi:10.1016/j.calphad.2009.07.004.
- [48] D. Rodney, G. Martin, Dislocation pinning by glissile interstitial loops in a nickel crystal: A molecular-dynamics study, *Physical Review B* 61 (13) (2000) 8714–8725. doi:10.1103/PhysRevB.61.8714.
- [49] M. X. Zhang, P. M. Kelly, Edge-to-edge matching and its applications: Part II. Application to Mg-Al, Mg-Y and Mg-Mn alloys, *Acta Materialia* 53 (4) (2005) 1085–1096. doi:10.1016/j.actamat.2004.11.005.
- [50] W. Xiao, X. Zhang, W. T. Geng, G. Lu, Atomistic study of plastic deformation in Mg-Al alloys, *Materials Science and Engineering A* 586 (2013) 245–252. doi:10.1016/j.msea.2013.07.093.
- [51] K. Hagihara, K. Hayakawa, Plastic deformation behavior and operative slip systems in $Mg_{17}Al_{12}$ single crystals, *Materials Science and Engineering: A* 737 (2018) 393–400.
- [52] B. A. Szajewski, W. A. Curtin, Analysis of spurious image forces in atomistic simulations of dislocations, *Modelling and Simulation in Materials Science and Engineering* 23 (2) (2015) 025008. doi:10.1088/0965-0393/23/2/025008.
- [53] D. Sheppard, R. Terrell, G. Henkelman, Optimization methods for finding minimum energy paths., *The Journal of chemical physics* 128 (13) (2008) 134106. doi:10.1063/1.2841941.
- [54] J. Guérolé, A. Vaid, F. Houllé, Z. Xie, W. G. Nöhring, A. Prakash, E. Bitzek, Assessment and optimization of the fast inertial relaxation engine (fire) for energy minimization in atomistic simulations and its implementation in lammmps, to be published.
- [55] E. Bitzek, P. Koskinen, F. Gähler, M. Moseler, P. Gumbsch, M. Moseler, P. Gumbsch, Structural Relaxation Made Simple, *Physical Review Letters* 97 (17) (2006) 170201. doi:10.1103/PhysRevLett.97.170201.
- [56] S. S. Nosé, A molecular dynamics method for simulations in the canonical ensemble, *Molecular Physics* 52 (2) (1984) 255–268. doi:10.1080/00268978400101201.
- [57] H. W. G., W. G. Hoover, Canonical Dynamics: Equilibrium Phase-Space Distributions, *Phys. Rev. A: At., Mol., Opt. Phys.* 31 (3) (1985) 1695. doi:10.1103/PhysRevA.31.1695.
- [58] W. G. Hoover, Constant-pressure equations of motion, *Physical Review A* 34 (3) (1986) 2499–2500. arXiv:arXiv:1011.1669v3,

- [doi:10.1103/PhysRevA.34.2499](https://doi.org/10.1103/PhysRevA.34.2499).
- [59] A. Stukowski, Visualization and analysis of atomistic simulation data with OVITO—the Open Visualization Tool, *Modelling and Simulation in Materials Science and Engineering* 18 (1) (2010) 015012. [doi:10.1088/0965-0393/18/1/015012](https://doi.org/10.1088/0965-0393/18/1/015012).
- [60] D. Faken, H. Jónsson, Systematic analysis of local atomic structure combined with 3D computer graphics, *Computational Materials Science* 2 (2) (1994) 279–286. [doi:10.1016/0927-0256\(94\)90109-0](https://doi.org/10.1016/0927-0256(94)90109-0).
- [61] J. D. Honeycutt, H. C. Andersen, Molecular Dynamics Study of Melting and Freezing of Small Lennard-Jones Clusters, *Journal of Physical Chemistry* 91 (24) (1987) 4950–4963. [doi:10.1021/j100303a014](https://doi.org/10.1021/j100303a014).
- [62] A. P. Thompson, S. J. Plimpton, W. Mattson, General formulation of pressure and stress tensor for arbitrary many-body interaction potentials under periodic boundary conditions, *The Journal of Chemical Physics* 131 (15) (2009) 154107. [doi:10.1063/1.3245303](https://doi.org/10.1063/1.3245303).
- [63] M. Zhou, A new look at the atomic level virial stress: on continuum-molecular system equivalence, *Proceedings of the Royal Society A: Mathematical, Physical and Engineering Sciences* 459 (2037) (2003) 2347–2392. [doi:10.1098/rspa.2003.1127](https://doi.org/10.1098/rspa.2003.1127).
- [64] M. P. Allen, D. J. Tildesley, *Computer Simulation of Liquids*, Oxford Science Publ, Clarendon Press, 1989.
- [65] A. P. Sutton, *Interfaces in crystalline materials*, Monographs on the Physics and Chemistry of Materials (1995) 414–423.
- [66] D. Wolf, V. Yamakov, S. Phillpot, A. Mukherjee, H. Gleiter, Deformation of nanocrystalline materials by molecular-dynamics simulation: relationship to experiments?, *Acta Materialia* 53 (1) (2005) 1–40.
- [67] M. Dao, L. Lu, R. Asaro, J. T. M. De Hosson, E. Ma, Toward a quantitative understanding of mechanical behavior of nanocrystalline metals, *Acta Materialia* 55 (12) (2007) 4041–4065.
- [68] J. Wang, R. Hoagland, X. Liu, A. Misra, The influence of interface shear strength on the glide dislocation–interface interactions, *Acta Materialia* 59 (8) (2011) 3164–3173.
- [69] E. Bitzek, C. Brandl, D. Weygand, P. Derlet, H. Van Swygenhoven, Atomistic simulation of a dislocation shear loop interacting with grain boundaries in nanocrystalline aluminium, *Modelling and Simulation in Materials Science and Engineering* 17 (5) (2009) 055008.
- [70] R. Wang, A. Eliezer, E. Gutman, Microstructures and dislocations in the stressed AZ91D magnesium alloys, *Materials Science and Engineering: A* 344 (1-2) (2003) 279–287.
- [71] C. R. Hutchinson, J.-F. Nie, S. Gorsse, Modeling the precipitation processes and strengthening mechanisms in a mg-al-(zn) az91 alloy, *Metallurgical and Materials Transactions A* 36 (8) (2005) 2093–2105.
- [72] J. P. Hirth, J. Lothe, *Theory of dislocations* (second edition), second edition Edition, John Wiley & Sons, Inc, 1982. [doi:10.1016/0502-8205\(53\)90018-5](https://doi.org/10.1016/0502-8205(53)90018-5).
- [73] H. Mathur, V. Maier-Kiener, S. Korte-Kerzel, Deformation in the γ -Mg₁₇Al₁₂ phase at 25–278° c, *Acta Materialia* 113 (2016) 221–229.
- [74] M. Fukuchi, K. Watanabe, Temperature and composition dependence of hardness, resistivity and thermoelectric power of the gamma-phase in the aluminum-magnesium system, *Nippon Kinzoku Gakkaishi* 39 (5) (1975) 493–498.
- [75] K. Edalati, Z. Horita, Correlations between hardness and atomic bond parameters of pure metals and semi-metals after processing by high-pressure torsion, *Scripta Materialia* 64 (2) (2011) 161–164.
- [76] K. Song, H. Fujii, K. Nakata, Effect of welding speed on microstructural and mechanical properties of friction stir welded Inconel 600, *Materials & Design* 30 (10) (2009) 3972–3978. [doi:10.1016/j.matdes.2009.05.033](https://doi.org/10.1016/j.matdes.2009.05.033).
- [77] J. Ragani, P. Donnadieu, C. Tassin, J. J. Blandin, High-temperature deformation of the γ -Mg₁₇Al₁₂ complex metallic alloy, *Scripta Materialia* 65 (3) (2011) 253–256. [doi:10.1016/j.scriptamat.2011.04.022](https://doi.org/10.1016/j.scriptamat.2011.04.022).
- [78] M. Maghsoudi, A. Zarei-Hanzaki, H. Abedi, A. Shamsolhodaei, The evolution of γ -Mg₁₇Al₁₂ intermetallic compound during accumulative back extrusion and subsequent ageing treatment, *Philosophical Magazine* 95 (31) (2015) 3497–3523.
- [79] M. Kolb, C. Walther, J. Wheeler, S. Korte, W. Clegg, Private communications, to be published.
- [80] D. J. Bacon, U. F. Kocks, R. O. Scattergood, The effect of dislocation self-interaction on the orowan stress, *Philosophical Magazine* 28 (6) (1973) 1241–1263. [doi:10.1080/14786437308227997](https://doi.org/10.1080/14786437308227997).
- [81] R. O. Scattergood, D. J. Bacon, The strengthening effect of voids, *Acta Metallurgica* 30 (8) (1982) 1665–1677. [doi:10.1016/0001-6160\(82\)90188-2](https://doi.org/10.1016/0001-6160(82)90188-2).
- [82] F. Wang, B. Li, Atomistic calculations of surface and interfacial energies of Mg₁₇Al₁₂–Mg system, *Journal of magnesium and alloys*.
- [83] A. Kelly, R. Nicholson, *Strengthening methods in crystals*, Materials science series, Applied Science, 1971.
- [84] H. C. Thomas, *Mechanical behavior of materials*, 2000.
- [85] J. Fisher, E. W. Hart, R. Pry, The hardening of metal crystals by precipitate particles, *Acta Metallurgica* 1 (3) (1953) 336–339.
- [86] H. Gao, L. Zhang, S. P. Baker, Dislocation core spreading at interfaces between metal films and amorphous substrates, *Journal of the Mechanics and Physics of Solids* 50 (10) (2002) 2169–2202.
- [87] Z. Huang, J. E. Allison, A. Misra, Interaction of glide dislocations with extended precipitates in mg-nd alloys, *Scientific reports* 8 (1) (2018) 3570.
- [88] D. Srolovitz, M. Luton, R. Petkovic-Luton, D. Barnett, W. Nix, Diffusionally modified dislocation-particle elastic interactions, *Acta Metallurgica* 32 (7) (1984) 1079–1088.
- [89] W. Blum, B. Reppich, B. Wilshire, R. Evans, *Progress in creep and fracture* (1985).

Supplementary material to Atomistic Simulations of Basal Dislocations Interacting with Mg₁₇Al₁₂ Precipitates in Mg

Aviral Vaid ^a, Julien Guénoilé ^{b, a}, Aruna Prakash ^{c, a}, Sandra Korte-Kerzel ^b, Erik Bitzek ^a

^a Department of Materials Science and Engineering, Institute I, Friedrich-Alexander Universität Erlangen-Nürnberg (FAU), Martensstr. 5, 91058 Erlangen, Germany

^b Institute of Physical Metallurgy and Metal Physics, RWTH Aachen University, Germany

^c Micromechanical Materials Modelling (MiMM), Institute of Mechanics and Fluid Dynamics, Technische Universität Bergakademie Freiberg (TUBAF), Germany

Table of Content

S1. Comparison of Interatomic Potentials	1
S2. Interface termination of Mg ₁₇ Al ₁₂ Embedded in Mg Matrix	4
S3. Influence of Simulation Box Size on the Critical Resolved Shear Stress.....	5
S4. Dislocation Precipitate Interaction using NVT at $T = 300$ K.....	7
S5. Interface Width of Mg ₁₇ Al ₁₂ Embedded in Mg Matrix.....	7
S6. Anisotropic Shear Modulus	6
References.....	13

S1. Comparison of Interatomic Potentials

Studying the interaction of dislocations in magnesium with Mg₁₇Al₁₂ precipitate requires potentials that properly describe the pure Mg phase and the intermetallic phase Mg₁₇Al₁₂. To our knowledge, such potentials are:

- EAM potential by Liu *et. al* [1]
- MEAM potential by Jelinek *et. al* [2]
- MEAM potential by Kim *et. al* [3]
- MEAM potential by Jelinek *et. al* [4]

Pasianot and Savino had previously reported that the embedded atom method (EAM) formalism falls short in aptly describing the elastic constants of pure hcp metals [5]. Therefore, the first potential in the list above was ignored. The modified EAM (MEAM) potential by Jelinek *et. al* (2007) [2] specifically states that it is unsuitable to study the intermetallic Mg₁₇Al₁₂ phase and was thus also not considered.

To test the remaining potentials, several simulations were performed on model systems to compute material properties, such as lattice parameter, elastic constants, *etc.* for both Mg and Mg₁₇Al₁₂. For Mg, the X-, Y- and Z-axis were along $[2\bar{1}\bar{1}0]$, $[01\bar{1}0]$ and $[0001]$ respectively, while for Mg₁₇Al₁₂, these axes were along $[100]$, $[010]$ and $[001]$ respectively.

- The lattice parameter and cohesive energy were determined from relaxing a setup containing $5 \times 5 \times 5$ unit cells with periodic boundary conditions (PBC) in all directions.

- The elastic constants were calculated using the `Elastic` script from the LAMMPS package – the setup in this case also contained $5 \times 5 \times 5$ unit cells with PBC in all directions. The script calculates all elastic constants for a general anisotropic material by applying appropriate strains and measuring the resulting stresses. C_{11} , C_{12} , C_{13} , C_{33} , C_{44} were calculated as the averages of corresponding symmetry equivalent components.
- To compute the surface energy of the basal plane of Mg, the simulation cell contained $5 \times 5 \times 5$ unit cells with fixed boundary conditions on the basal plane and PBC in the other directions. The setup was then minimized to a force norm of 10^{-8} eV/Å using FIRE [6]. The surface energy was computed to be $(E - N \times E_{coh})/A$, where E is the total energy of the system with the surface, N is the number of atoms, E_{coh} is the cohesive energy of Mg and A is the surface area of the basal plane.
- The vacancy formation energy of Mg was computed by removing one atom in a setup that contained $5 \times 5 \times 5$ unit cells with PBC in all directions, and to subsequently minimized it to a force norm of 10^{-8} eV/Å.

A comparison between the potential properties for the remaining two potentials is shown in tables below.

Property (Mg)	Experiment/ Ab-initio	Jelinek 2012	Kim 2009
Cohesive Energy [eV/atom]	-1.55 [7]	-1.51	-1.55
Lattice Constant [Å]	3.209 [8]	3.202	3.209
c/a ratio	1.623 [8]	1.620	1.619
Bulk Modulus [GPa]	36.9 [9]	35.71	36.98
C_{11} [GPa]	63.5 [9]	59.43	62.99
C_{12} [GPa]	25.9 [9]	23.18	26.03
C_{13} [GPa]	21.7 [9]	23.76	21.23
C_{33} [GPa]	66.5 [9]	61.18	69.82
C_{44} [GPa]	18.4 [9]	17.37	17.20
Surface Energy $\gamma_{(0001)}$ [mJ/m ²]	785 [10]	716.21	677.5
Vacancy Formation Energy [eV]	0.91 [11]	0.44	0.89

Property (Mg ₁₇ Al ₁₂)	Experiment/ Ab-initio	Jelinek 2012	Kim 2009
Enthalpy of Formation [meV/atom]	-17.0 [2]	49.4	-18.5
Lattice Constant [Å]	10.55 [12]	10.73	10.56
Bulk Modulus [GPa]	48.3 [12]	47.6	49.5
C_{44} [GPa]	20.0 [12]	-2.3	13.6
$(C_{11}-C_{12})/2$ [GPa]	28.9 [12]	35.4	25.8

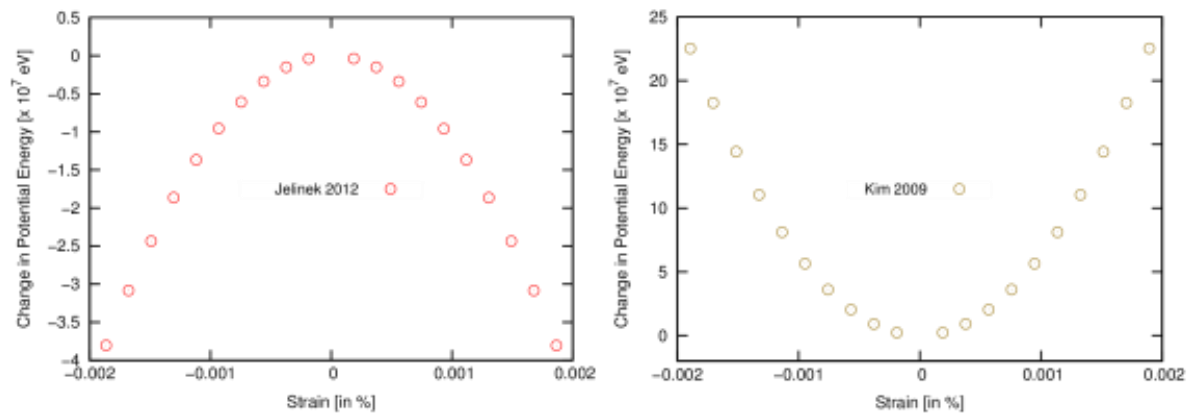


Figure S1: Change in potential energy of an $\text{Mg}_{17}\text{Al}_{12}$ sample with applied shear strain

The potential by Jelinek *et. al* [4] did not report any elastic constants. However, the ones computed using the methodology described above reported negative value of the elastic constant C_{44} for the intermetallic $\text{Mg}_{17}\text{Al}_{12}$, which is physically unfeasible. This aberration is also shown in the fig. S1, where the change in potential energy of the setup is plotted against applied shear strain. In addition to predicting a negative elastic constant, the potential also records a positive enthalpy of formation for $\text{Mg}_{17}\text{Al}_{12}$ contrary to the experimental [13] and *ab-initio* [12] studies showing it to be a stable phase. Therefore, this potential was also excluded from our list of potentials. The potential properties of the potential by Kim *et. Al* [3] were found to be reproducible and therefore chosen as the potential of choice for further investigation in this work.

S2. Interface termination of Mg₁₇Al₁₂ Embedded in Mg Matrix

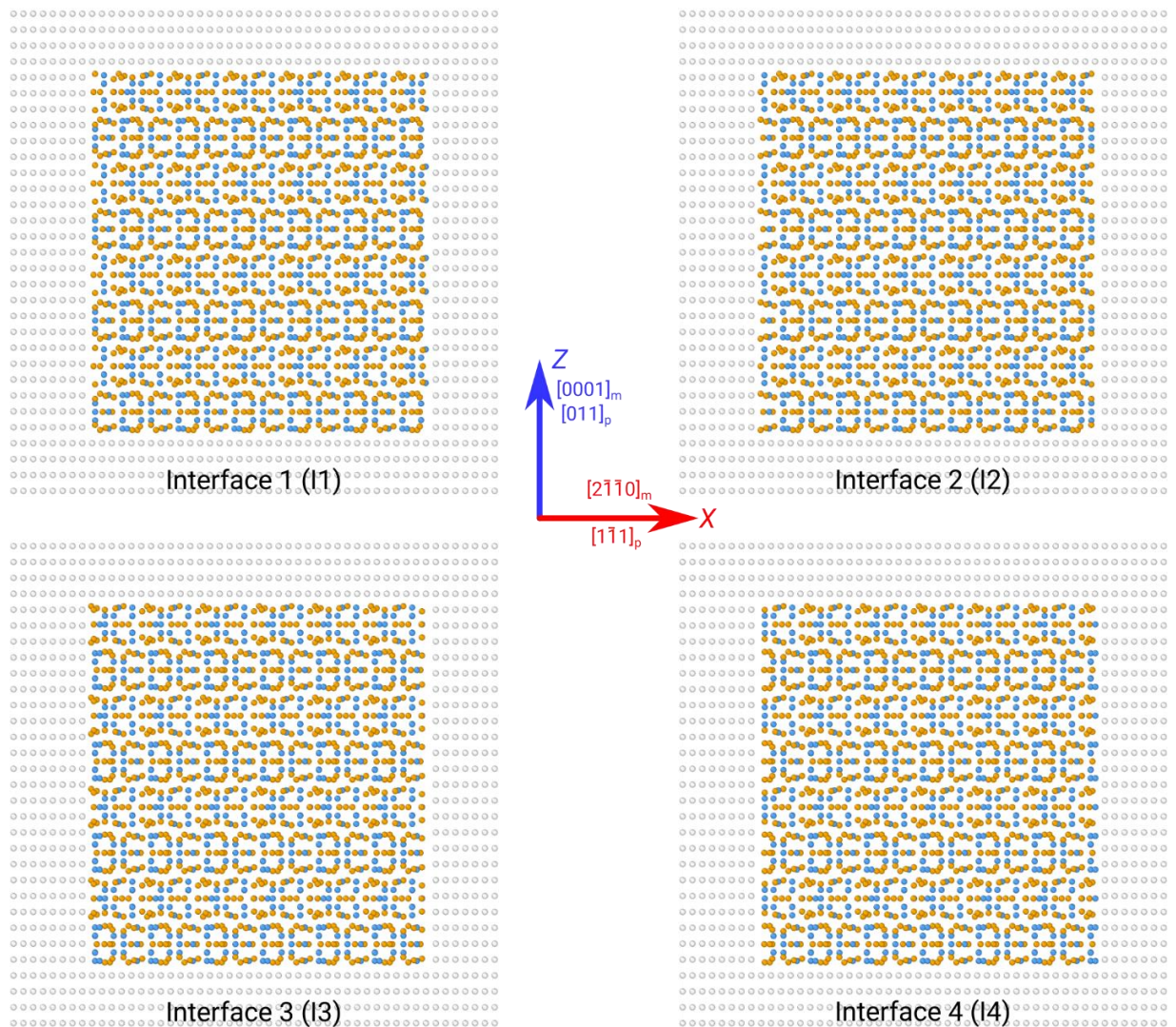


Figure S2: Different interface terminations of the Mg₁₇Al₁₂ precipitate (orange: Mg, blue Al) embedded in the Mg matrix (grey atoms) studied in the present work. The interface number correspond to those presented in the Fig. 1 of the main manuscript.

S3. Influence of Simulation Box Size on the Critical Resolved Shear Stress

The following table shows the computed critical resolved shear stress, τ_C along with the simulation cell dimensions. No other parameters were modified other than the box aspect ratio (L_X/L_Z), which was shown to be the critical parameter to minimize the influence of spurious image forces [14], as compared to the *default setup*. According to Szajewski and Curtin [14], an aspect ratio of $1/\sqrt{2}$ would minimize the spurious image forces for an edge dislocation. As seen from the table below, the effect of these image forces is not significant in our simulations.

Sample Name	L_X [Å]	L_Y [Å]	L_Z [Å]	(L_X/L_Z)	L [Å]	D [Å]	τ_C [MPa]
<i>Default setup</i>	400	200	200	2	122	78	245 ± 5
Alt. setup 1	500	200	200	2.5	122	78	235 ± 5
Alt. setup 2	400	200	500	0.8	122	78	245 ± 5

S4. Anisotropic Shear Modulus

The anisotropic shear modulus was calculated using the LAMMPS package – the setup in this case contained $5 \times 5 \times 5$ unit cells with periodic boundary conditions in all directions. For Mg, the X-, Y- and Z-axis were along $[2\bar{1}\bar{1}0]$, $[01\bar{1}0]$ and $[0001]$ respectively, while for Mg₁₇Al₁₂, these axes were along $[1\bar{1}\bar{1}]$, $[21\bar{1}]$ and $[011]$ respectively. The elastic constants were calculated using the `Elastic` script from the LAMMPS package. The script calculates all elastic constants for a general anisotropic material by applying appropriate strains and measuring the resulting stresses. The anisotropic shear modulus was calculated as the averages of corresponding symmetry equivalent components.

$$\mu' (Mg) = 17.2 \text{ GPa}$$

$$\mu' (Mg_{17}Al_{12}) = 17.6 \text{ GPa}$$

S5. Interface Width of $\text{Mg}_{17}\text{Al}_{12}$ Embedded in Mg Matrix

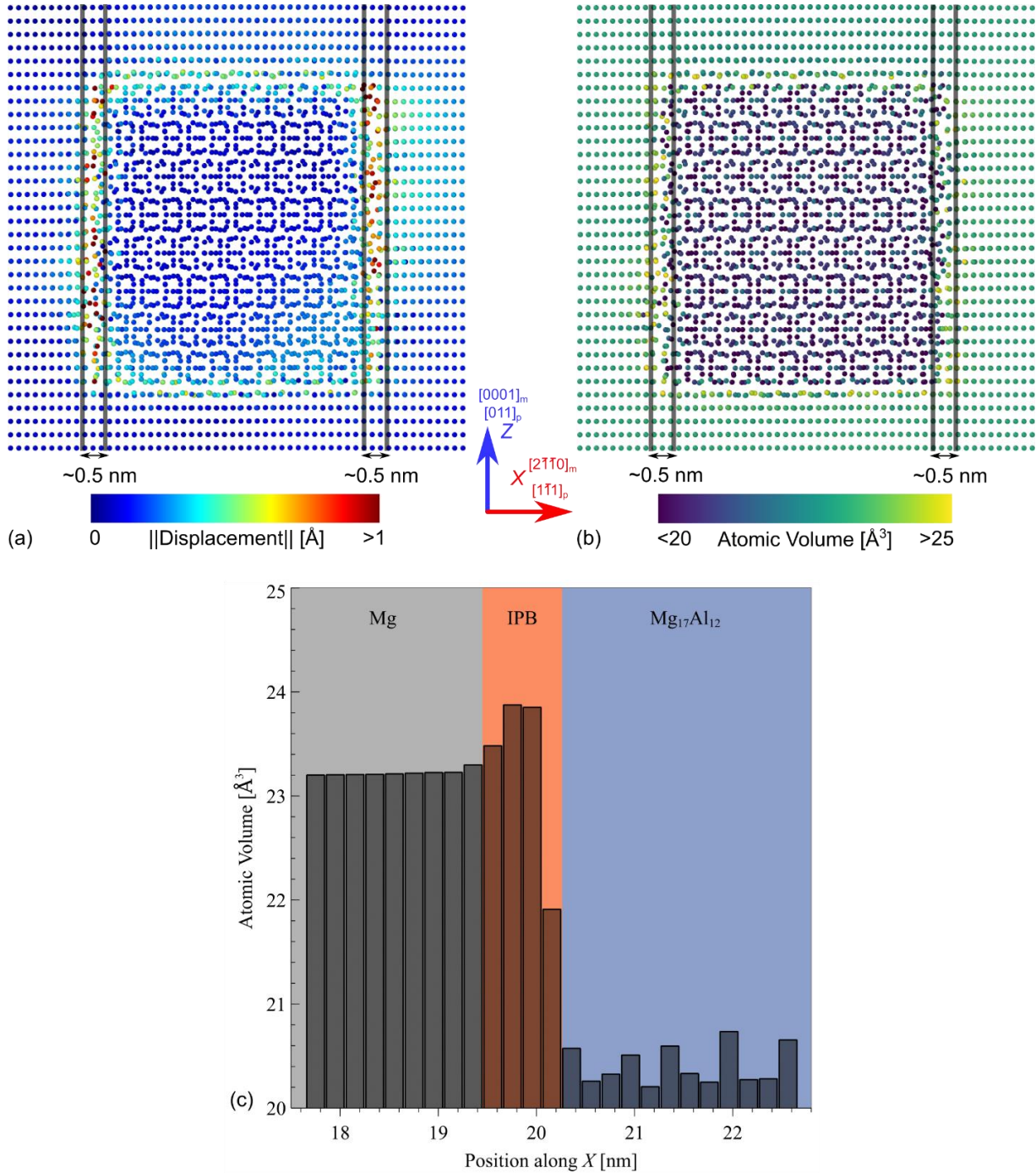


Figure S3: Side view showing the width of the Mg- $\text{Mg}_{17}\text{Al}_{12}$ interface for a relaxed precipitate in the matrix following the Burgers orientation relationship computed using (a) Displacement magnitude with respect to the perfect lattice positions, and (b) atomic volume. (c) Histogram of atomic volume for the region around the left interface with a binning width of 2\AA showing an increased excess volume.

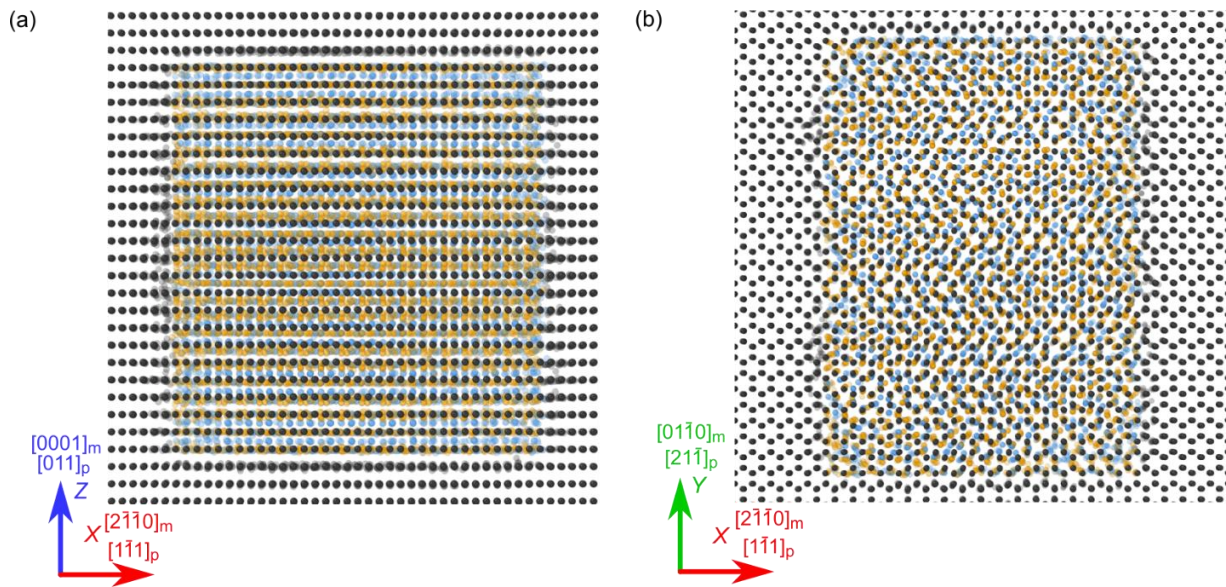


Figure S4: (a) Side view and (b) top view showing the local disordered region at the Mg-Mg₁₇Al₁₂ IPB for a relaxed precipitate in the matrix following the Burgers orientation relationship. The matrix atoms are dark grey, while the atoms in the precipitate are colored based on atomic species – Mg (orange), Al (blue).

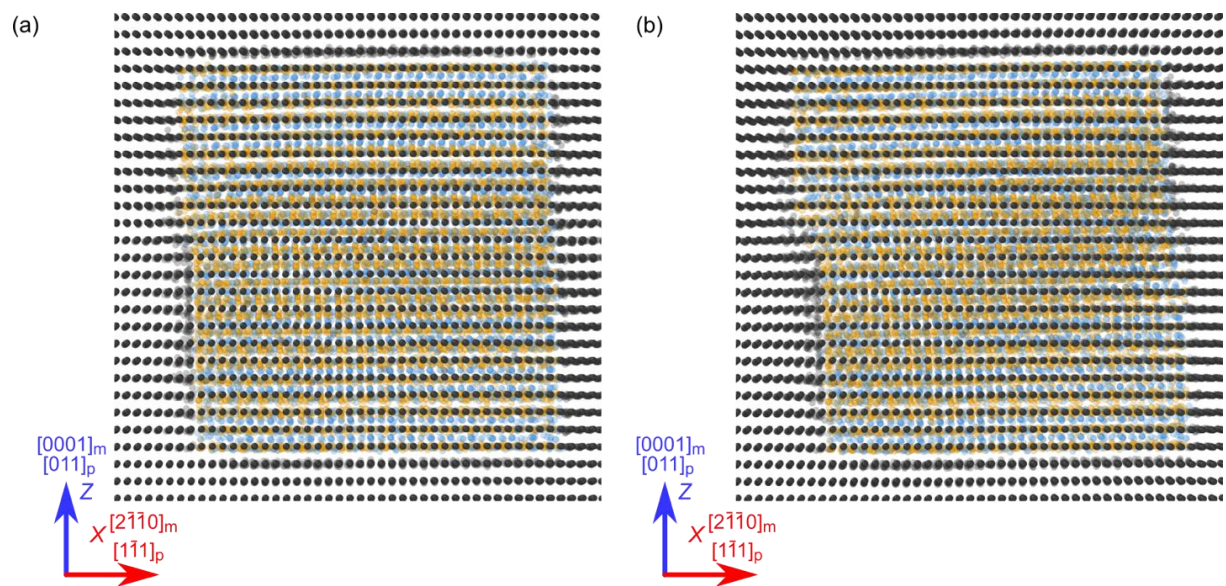


Figure S5: Side view showing the relaxed local disordered region at the Mg-Mg₁₇Al₁₂ IPB for the *default setup* (a) with one absorbed dislocation at $\tau = 240$ MPa, (b) with two absorbed dislocations after passage of the first dislocation at $\tau = 250$ MPa. The matrix atoms are dark grey, while the atoms in the precipitate are colored based on atomic species – Mg (orange), Al (blue).

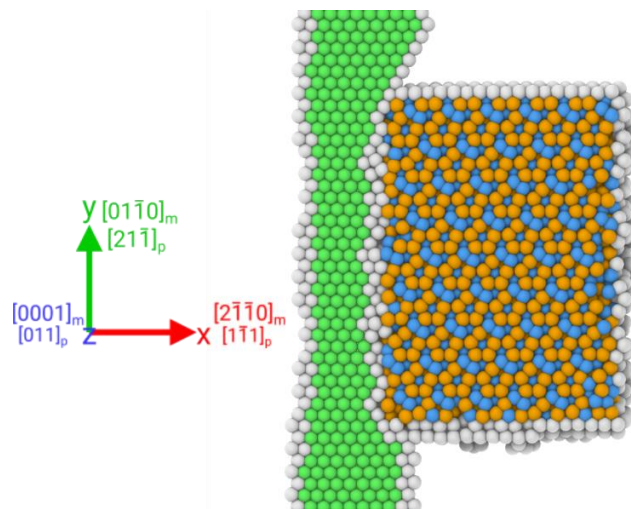


Figure S6: Top view of a cut just above the dislocation glide plane showing an edge dislocation in front of the precipitate upon energy minimization at $\tau = 0$ MPa for the *default setup*. The defect atoms in the Mg matrix are colored as green (fcc) and white (other), while the atoms in the precipitate are colored based on atomic species – Mg (orange), Al (blue). The hcp coordinated matrix atoms are not shown.

S6. Dislocation Precipitate Interaction using NVT at $T = 300$ K

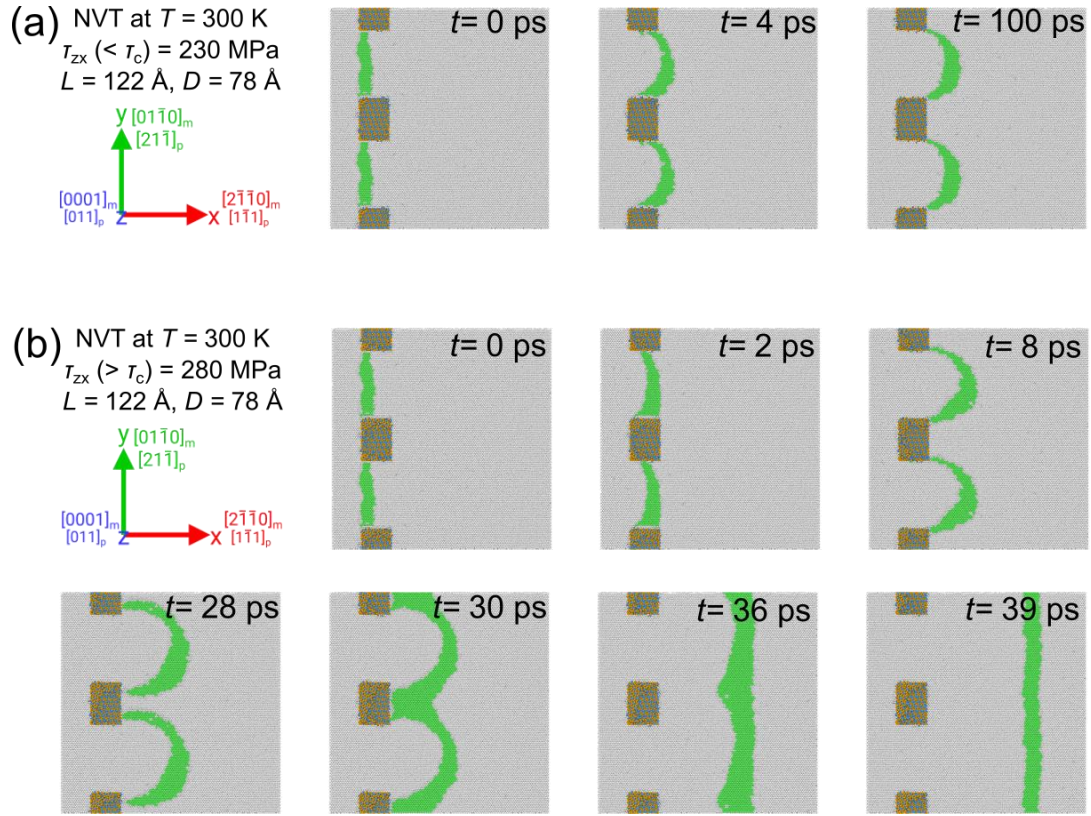


Figure S7: Infinite basal edge dislocation interacting with a periodic array of $Mg_{17}Al_{12}$ precipitates using molecular dynamics NVT simulation at $T = 300$ K with an applied shear stress (a) smaller, and (b) larger than the critical resolved shear stress ($L = 122$ Å, $D = 78$ Å). The Mg atoms in the matrix are colored grey and the defect fcc atoms in the Mg matrix green, while the atoms in the precipitate are colored based on atomic species – Mg (orange), Al (blue).

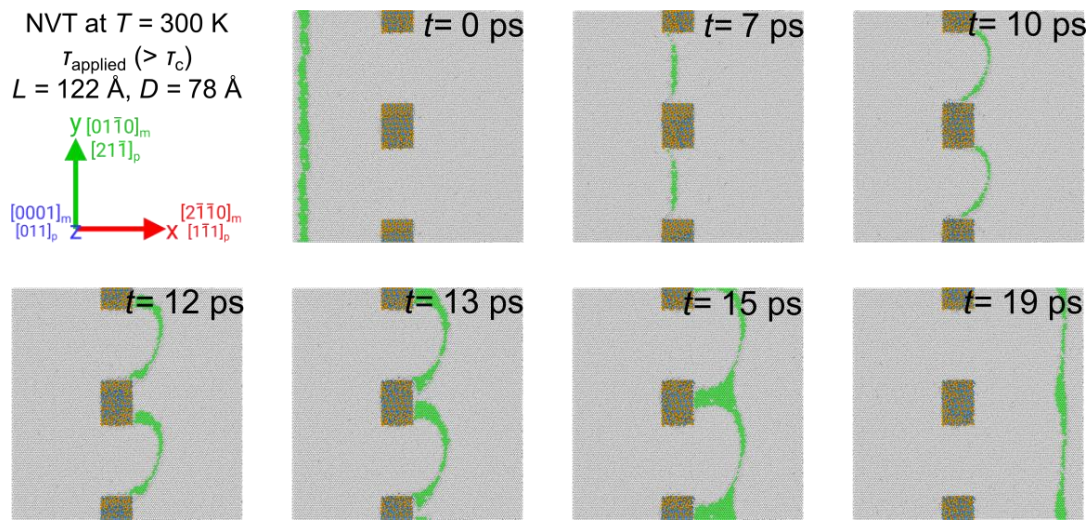


Figure S8: Infinite 30° mixed dislocation interacting with a periodic array of $\text{Mg}_{17}\text{Al}_{12}$ precipitates using molecular dynamics NVT simulation at $T = 300$ K with an applied shear stress larger than the critical resolved shear stress ($L = 122\text{\AA}$, $D = 78\text{\AA}$). The Mg atoms in the matrix are colored grey and the defect fcc atoms in the Mg matrix green, while the atoms in the precipitate are colored based on atomic species – Mg (orange), Al (blue).

S7. Unloading the simulation cell

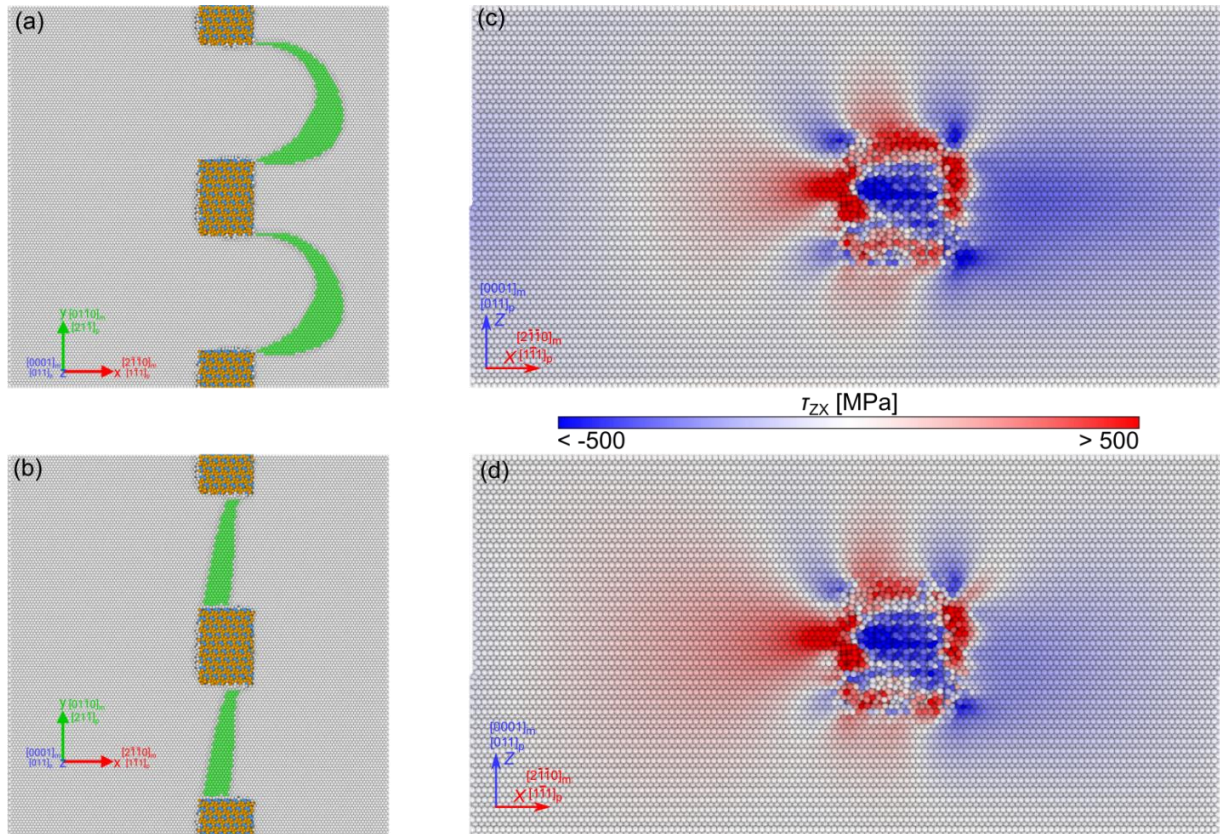


Figure S9: Top view of a relaxed dislocation (a) before and (b) after unloading the simulation cell for the *default* setup that was previously loaded at $\tau (< \tau_c) = 240$ MPa. (c) and (d) show the corresponding stress states from the side view. The color code for (a) and (b) is as follows: The Mg atoms in the matrix are colored grey and the defect fcc atoms in the Mg matrix green, while the atoms in the precipitate are colored based on atomic species – Mg (orange), Al (blue). The color code for the stress state is shown in the figure.

References:

- [1] X.Y. Liu, P.P. Ohotnicky, J.B. Adams, C. Lane Rohrer, R.W. Hyland, Anisotropic surface segregation in Al-Mg alloys, *Surf. Sci.* 373 (1997) 357–370. doi:10.1016/S0039-6028(96)01154-5.
- [2] B. Jelinek, J. Houze, S. Kim, M.F. Horstemeyer, M.I. Baskes, S.G. Kim, Modified embedded-atom method interatomic potentials for the Mg-Al alloy system, *Phys. Rev. B - Condens. Matter Mater. Phys.* 75 (2007) 1–9. doi:10.1103/PhysRevB.75.054106.
- [3] Y.M. Kim, N.J. Kim, B.J. Lee, Atomistic Modeling of pure Mg and Mg-Al systems, *Calphad Comput. Coupling Phase Diagrams Thermochem.* 33 (2009) 650–657. doi:10.1016/j.calphad.2009.07.004.
- [4] B. Jelinek, S. Groh, M.F. Horstemeyer, J. Houze, S.G. Kim, G.J. Wagner, A. Moitra, M.I. Baskes, Modified embedded atom method potential for Al, Si, Mg, Cu, and Fe alloys, *Phys. Rev. B - Condens. Matter Mater. Phys.* 85 (2012). doi:10.1103/PhysRevB.85.245102.
- [5] R. Pasianot, E.J. Savino, Embedded-atom-method interatomic potentials for hcp metals, *Phys. Rev. B.* 45 (1992) 12704–12710. doi:10.1103/PhysRevB.45.12704.
- [6] J. Guénoilé, A. Vaid, F. Houllé, Z. Xie, W.G. Nöhring, A. Prakash, E. Bitzek, Assessment and optimization of the fast inertial relaxation engine (fire) for energy minimization in atomistic simulations and its implementation in lammmps, *To Be Publ.* (2019).
- [7] M.I. Baskes, R.A. Johnson, Modified embedded atom potentials for HCP metals, *Model. Simulations Mater. Sci. Eng.* 2 (1994) 147–163.
- [8] C.S. Barrett, T.B. Massalski, *Structure of Metals: Crystallographic Methods, Principles And Data*, Pergamon Press, Oxford, 1980.
- [9] G. Simmons, *Single crystal elastic constants and calculated aggregate properties: A Handbook*, SOUTHERN METHODIST UNIV DALLAS TEX, 1965.
- [10] W.R. Tyson, W.A. Miller, Surface free energies of solid metals: Estimation from liquid surface tension measurements, *Surf. Sci.* (1977). doi:10.1016/0039-6028(77)90442-3.
- [11] N. Chetty, M. Weinert, T.S. Rahman, J.W. Davenport, Vacancies and impurities in aluminum and magnesium, *Phys. Rev. B.* (1995). doi:10.1103/PhysRevB.52.6313.
- [12] N. Wang, W.Y. Yu, B.Y. Tang, L.M. Peng, W.J. Ding, Structural and mechanical properties of Mg₁₇Al₁₂ and Mg₂₄Y₅ from first-principles calculations, *J. Phys. D. Appl. Phys.* 41 (2008). doi:10.1088/0022-3727/41/19/195408.
- [13] J.A. Brown, J.A. Brown, D. Laboratories, S. Park, *The Thermodynamic Properties of Solid Al-Mg Alloys*, 1 (1970).
- [14] B.A. Szajewski, W.A. Curtin, Analysis of spurious image forces in atomistic simulations of dislocations, *Model. Simul. Mater. Sci. Eng.* 23 (2015). doi:10.1088/0965-0393/23/2/025008.